



UNIVERSIDAD DE CHILE  
FACULTAD DE CIENCIAS FÍSICAS Y MATEMÁTICAS  
DEPARTAMENTO DE INGENIERÍA ELÉCTRICA

CCAT-PRIME TELESCOPE HOLOGRAPHY SIMULATIONS AND SURFACE ERROR  
ANALYSIS.

TESIS PARA OPTAR AL GRADO DE MAGÍSTER EN CIENCIAS DE LA  
INGENIERÍA, MENCIÓN ELÉCTRICA

MEMORIA PARA OPTAR AL TÍTULO DE INGENIERA CIVIL ELÉCTRICA

CATALINA MEDINA PORCILE

PROFESOR GUÍA:  
NICOLÁS ANDRÉS REYES GUZMÁN

MIEMBROS DE LA COMISIÓN:  
FAUSTO PATRICIO MENA MENA  
ROLANDO DÜNNER PLANELLA

Este trabajo ha sido parcialmente financiado por el proyecto QUIMAL 180004

SANTIAGO DE CHILE  
2019

Resumen de la Tesis para optar  
al grado de Magíster en Ciencias  
de la Ingeniería, Mención Eléctrica.  
Por: Catalina Medina.  
Fecha:2019  
Prof.Guía: Nicolás Reyes

## CCAT-PRIME TELESCOPE HOLOGRAPHY SIMULATIONS AND SURFACE ERROR ANALYSIS.

El radio-telescopio CCAT-prime (CCAT-p) será construido en el Cerro Chajnantor a 5.600 m.s.n.m en la Región de Antofagasta, Chile. Este telescopio tendrá una configuración Crossed-Dragone con dos reflectores de 6 m. Esta configuración le otorga un amplio campo de visión con el que podrá iluminar más de  $10^5$  detectores.

El rango de operación del CCAT-p comprende longitudes de onda desde los  $350 \mu\text{m}$  hasta los  $3.100 \mu\text{m}$ , y en las mejores condiciones climáticas podrá llegar hasta la ventana de  $200 \mu\text{m}$ . Para operar a estas longitudes de onda se necesita que la superficie de los reflectores tenga una alta precisión, por lo que se ha impuesto una meta para el error medio de frente de ondas entre  $7$  y  $10 \mu\text{m}$  RMS.

Los reflectores del telescopio serán construidos mediante un set de paneles que en conjunto conformarán el perfil deseado. Para lograr la precisión requerida, se necesitará implementar un método de medición de errores en la superficie de los reflectores. Se ha escogido con este fin la técnica de holografía de ondas milimétricas.

La implementación de técnicas de holografía para el CCAT-p presenta desafíos, debido principalmente a su ubicación, a su configuración óptica y al alto nivel de precisión deseado. Se utilizará una fuente artificial a  $300$  m del telescopio, lo cual corresponde a su campo cercano, por lo que se necesita estudiar el comportamiento del patrón de radiación a esta distancia. En este trabajo se hacen simulaciones tanto en campo cercano como en campo lejano, bajo distintos escenarios, para así generar datos del comportamiento del telescopio ante estas circunstancias. Por otro lado, ya que el telescopio consta de dos grandes reflectores, el error medido por el sistema de holografía corresponderá a las contribuciones de los errores en la superficie de cada reflector. Para identificar y separar la contribución de cada reflector se propone utilizar los efectos de paralaje sobre la ubicación de los errores producidos al medir en distintas posiciones del plano focal. En este trabajo cada simulación se mide en  $4$  posiciones distintas del plano focal.

Mediante software se generan mapas de error para los distintos escenarios. Con esto se encuentra que los errores en el reflector secundario experimentan un cambio considerablemente mayor en su posición en la apertura, al cambiar la posición de medición en el plano focal, en comparación con los errores en el primario.

La holografía del CCAT-p ha sido simulada satisfactoriamente y se ha identificado un comportamiento diferente entre los errores de las superficies de los reflectores.

RESUMEN DE LA TESIS PARA OPTAR  
AL GRADO DE MAGÍSTER EN CIENCIAS  
DE LA INGENIERÍA, MENCIÓN ELÉCTRICA Y  
AL TÍTULO DE INGENIERA CIVIL ELÉCTRICA  
POR: CATALINA MEDINA PORCILE  
FECHA: 2019  
PROF. GUÍA: SR. NICOLÁS ANDRÉS REYES GUZMÁN  
PROF. CO-GUÍA: SR.

## CCAT-PRIME TELESCOPE HOLOGRAPHY SIMULATIONS AND SURFACE ERROR ANALYSIS.

The CCAT-prime (CCAT-p) radio telescope will be built on Cerro Chajnantor at 5,600 m.s.n.m in the Antofagasta Region, Chile. This telescope will have a Crossed-Dragone configuration with two 6 m reflectors. This configuration gives it a wide field of view and the capacity of illuminating more than  $10^5$  detectors.

The operational range of the CCAT-p goes from 350  $\mu\text{m}$  to 3,100  $\mu\text{m}$ , reaching the 200  $\mu\text{m}$  window under the best weather conditions. To operate at these wavelengths it is necessary that the surfaces of the reflectors have high accuracy. A 10–7  $\mu\text{m}$  RMS goal has been set for the half wavefront error.

The reflectors of the telescope will be built using a set of panels that together will arrange the desired profile. To achieve the required accuracy it will be necessary to implement an error measurement method for the surface of the reflectors. The millimeter wave holography technique has been chosen for this purpose.

Implementing holographic techniques for the CCAT-p presents challenges mainly due to its location and optics. An artificial source will be used at 300 m from the telescope, which is in its near field, so it is necessary to study the behavior of the radiation pattern at this distance. In this work, simulations are carried out both in the near field and in the far field, under different scenarios, in order to generate data on the behavior of the telescope in these circumstances. On the other hand, since the telescope consists of two large reflectors, the error measured by the holography system will correspond to the contributions of the errors on the surface of each reflector. For identifying and separating each reflector's contribution it is proposed to utilize the parallax effects over the errors locations that are produced by changing the measurement position at the focal plane. In this work each simulation is measured in 4 different positions of the focal plane.

Using software, the obtained results are analyzed and error maps are generated for the different scenarios. With this it is found that the errors in the secondary reflector change their location in the aperture considerably more than errors at the primary reflector depending on the measurement position.

The holography of CCAT-p has successfully been simulated and a different behaviour between the reflectors surface error has been identified.

*To my family, friends and teachers.*



# Contents

<b>List of Tables</b>	<b>vi</b>
<b>List of Figures</b>	<b>vii</b>
<b>1 Introduction</b>	<b>1</b>
1.0.1 Hypothesis . . . . .	3
1.0.2 Objectives . . . . .	3
1.0.3 The structure of this thesis . . . . .	4
<b>2 Bibliographic Review</b>	<b>5</b>
2.1 Crossed-Dragone Design . . . . .	5
2.2 Surface error . . . . .	6
2.3 Holography . . . . .	9
2.3.1 Far and near field . . . . .	10
2.3.2 Sampling and resolution . . . . .	11
2.3.3 Holography Accuracy . . . . .	12
2.4 Miscellaneous . . . . .	13
2.4.1 Imaging equation . . . . .	13
2.5 Summary . . . . .	13
<b>3 Design Parameters and Requirements</b>	<b>15</b>
3.1 CCAT-p optical design . . . . .	15
3.2 Holography Requirements . . . . .	17
3.2.1 Operating Frequency . . . . .	17
3.2.2 General Requirements . . . . .	18
3.2.3 Taking Data . . . . .	18
3.2.4 Source Location . . . . .	19
3.3 Summary . . . . .	19
<b>4 Simulations</b>	<b>21</b>
4.1 CCAT-P Simulations under different scenarios . . . . .	21
4.1.1 First scenario: Ideal surface CCAT-p simulations . . . . .	23
4.1.2 Second scenario: Error at MR surface . . . . .	25
4.1.3 Third scenario: Error at SR surface . . . . .	27
4.2 Conclusions . . . . .	27
<b>5 Processing and Analysis</b>	<b>31</b>

5.1	General Strategy . . . . .	31
5.2	Recovered illuminations and surface error maps . . . . .	32
5.2.1	First scenario: Ideal surfaces . . . . .	32
5.2.2	Second scenario: Error at MR surface . . . . .	33
5.2.3	Third scenario: Error at SR surface . . . . .	37
5.2.4	Fourth scenario: Synthetic scenario with errors at MR and SR surfaces	41
5.3	Compensating the RMS surface error . . . . .	44
5.4	Separation of errors . . . . .	48
5.5	Conclusions . . . . .	50
<b>6</b>	<b>Conclusions and future work</b>	<b>52</b>
6.1	Conclusions . . . . .	52
6.2	Future work . . . . .	53
<b>7</b>	<b>Bibliography</b>	<b>54</b>
<b>8</b>	<b>Appendix</b>	<b>57</b>

# List of Tables

2.1	Crossed-Dragone telescope geometry parameters. . . . .	7
3.1	CCAT-p optical design parameters. . . . .	16
5.1	Measured positions of the error at the MR depending on the feed location. .	36
5.2	Measured positions of the error at the SR depending on the feed location. . .	39
5.3	Measured positions of the errors at the MR and SR depending on the feed location for the fourth scenario. . . . .	45

# List of Figures

1.1	CCAT-p rendition by Vertex Antennentechnik GmbH [7]. . . . .	2
2.1	Crossed-Dragone parameters [18]. . . . .	8
2.2	Surface error. . . . .	9
2.3	Aperture and P(x,y) coordinate system. . . . .	10
2.4	Imaging equation [31]. . . . .	13
3.1	CCAT-p optical design [30]. All lengths are in mm. . . . .	17
3.2	Possible location of the holography source. . . . .	20
4.1	Four measuring positions at the focal plane. . . . .	23
4.2	CCAT-p model on GRASP software. Blue arrow is the z axis and red arrow is the x axis (scale is in meters). . . . .	23
4.3	Far-field diffraction pattern of the CCAT-p telescope. We show the polar and cross polar electric field obtained by simulations. . . . .	24
4.4	Electric field diffraction pattern of the CCAT-p telescope with the feed located at three off-axis positions. Simulations made at the far-field with ideal surfaces. . . . .	25
4.5	Phase of the electric field obtained for the three off-axis feed positions. . . . .	26
4.6	Near-field diffraction pattern for the telescope simulated with ideal surfaces. . . . .	27
4.7	Near-field diffraction patterns for the CCAT-p telescope with ideal surfaces. We show the patterns obtained for three off-axis positions of the feed. . . . .	28
4.8	Location of surface error at the MR (the error is not in scale). . . . .	29
4.9	Electric diffraction pattern of the CCAT-p telescope with errors at the MR surface. Far-field simulation. . . . .	29
4.10	Near-field diffraction pattern of the CCAT-p telescope with errors at the MR surface. . . . .	29
4.11	Location of surface error at the SR (the error is not in scale). . . . .	30
4.12	Far-field diffraction pattern of the CCAT-p when an error is introduced at the SR surface. . . . .	30
4.13	Near-field diffraction pattern obtained for the CCAT-p telescope with an error at the SR. . . . .	30
5.1	Amplitude and phase of the CCAT-p telescope obtained at the aperture for an ideal surface. . . . .	33
5.2	Amplitude and phase of the CCAT-p telescope obtained at the aperture for an ideal surface. Illumination with an off-axis feed. . . . .	33

5.3	Amplitude and phase of the CCAT-p telescope obtained at the aperture for a MR simulated with an error. . . . .	34
5.4	Amplitude and phase of the CCAT-p telescope obtained at the aperture for a MR simulated with an error. Illumination with an off-axis feed. . . . .	34
5.5	Surface error map obtained for the second scenario. . . . .	35
5.6	Surface error maps obtained for the second scenario with the feed off axis in three different positions. . . . .	36
5.7	Addition of the 4 surface error maps for the second scenario (surface error at MR). . . . .	37
5.8	Scheme of the surface error at MR and how rays reflects from one surface to another. $\theta_i$ is the angle of incidence at the bump surface . . . . .	37
5.9	Recovered illumination for the third scenario (error at the SR surface) in amplitude and phase. . . . .	38
5.10	Recovered illumination for the third scenario with the feed off-axis in three different positions. . . . .	38
5.11	Surface error map obtained for the third scenario. . . . .	39
5.12	Surface error maps for the third scenario. Shown for the three positions of the feed. . . . .	40
5.13	Addition of the 4 surface error maps for the third scenario (surface error at SR). . . . .	40
5.14	Scheme of the surface error at SR and how rays reflects from one surface to another. $\theta_i$ is the angle of incidence at the bump surface . . . . .	41
5.15	Far-field diffraction pattern obtained for the forth scenario in amplitude and phase. . . . .	42
5.16	Electric diffraction pattern obtained for the fourth scenario in amplitude and phase. . . . .	42
5.17	Illumination obtained for the phase scenario for the three positions of the feed. . . . .	43
5.18	Surface error map obtained for the forth scenario. . . . .	44
5.19	Addition of the 4 surface error maps for the synthetic scenario. . . . .	44
5.20	Surface error diminution algorithm. . . . .	46
5.21	Error maps obtained for each surface by calculating the mean between their correspondents surface error maps. . . . .	47
5.22	Surface error maps before applying the correction algorithm. . . . .	48
5.23	RMS surface error diminution by applying the algorithm for 30 iterations. . . . .	48
5.24	Surface error maps of each reflector after 30 iterations. . . . .	49
5.25	Rays at the aperture plane depending on the originating position in the focal plane [29]. . . . .	50

# Chapter 1

## Introduction

A large portion of the electromagnetic radiation that arrives to Earth corresponds to far-infrared and submillimeter radiation. It is mainly generated as thermal radiation from dust coming, for example, from star formation regions [1]. Water vapor of the atmosphere inhibits transmission of submillimeter wavelengths to the ground. Because of this, unique sites are required for studying this part of the electromagnetic spectrum [2]. The skies over the the Atacama desert in northern Chile have some of the best conditions for submillimeter astronomy, due to its combination of dryness and clearness given by the high elevation and low presence of clouds [3]. This is why some of the most powerful submillimeter observatories are located in this country, like the Atacama Large Millimeter/Submillimeter Array (ALMA) and the Atacama Pathfinder Experiment telescope (APEX).

The Atacama desert has also optimal conditions for optical telescopes, mainly given by the seeing of the sites. The Extremely large telescope (ELT) and Very Large telescope (VLT) are examples of big aperture optical telescopes located in here [4]. By 2020, Chile will concentrate the 70% of the world's telescope infrastructure [5].

High throughput telescopes enables large scale surveys of the sky, which is necessary, for example, for studying the remaining radiation from the early universe as the cosmic microwave background (CMB). Although current telescopes have the capacity of illuminating roughly  $10^4$  detectors, larger throughput telescopes are needed for illuminating next generation submillimeter and millimeter arrays, which will have  $10^5$  to  $10^6$  detectors [6].

The CCAT-prime (CCAT-p) radio telescope was born under both of this concerns, studying millimeter and submillimeter wavelengths with enough throughput for making large survey science. This will be achieved by its prime location, novel Crossed-Dragone configuration and high accuracy surface. In figure 1.1 an illustration of the telescope is shown.

The site of the telescope on Cerro Chajnantor at 5,600 m.s.n.m in the Antofagasta Region, Chile, will allow operations between the 350 to 3100  $\mu\text{m}$  wavelength range. The 200  $\mu\text{m}$  window can also be used under the best weather conditions. For a good performance at this wavelengths a high accuracy at the surface of the reflectors is needed. For an adequate

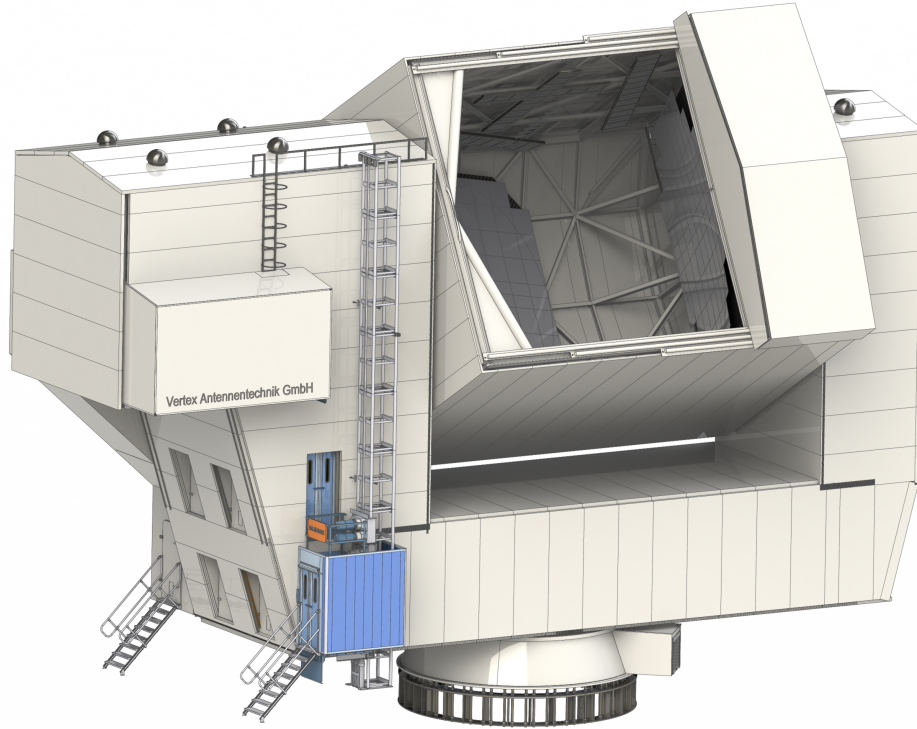


**Figure 1.1:** CCAT-p rendition by Vertex Antennentechnik GmbH [7].

performance a surface accuracy better than  $\frac{\lambda}{20}$  RMS is needed [8]. A goal of 7 to 10  $\mu\text{m}$  RMS has been set.

The CCAT-p will have two 6 m reflectors on a Crossed-Dragone configuration, which is an off-axis design with low blockage and a wide flat diffraction limited field of view (DL-FOV). This will deliver a high throughput, being able to illuminate  $> 10^5$  detectors. Other characteristics of this design includes a circularly symmetric radiation pattern and a very low cross-polarization [9].

The main science drivers of this telescope are: The kinematic Sunyaev-Zel'dovich effect, intensity mapping of [CII] from the epoch of reionization and the galactic ecology of the dynamic interstellar medium. It will also be a next-generation CMB observatory, due to its increased throughput and mapping velocity (10 times greater than current mapping velocities) [10]. For this, three preliminary instruments are in development: the submillimeter camera P-CAM, the heterodyne receiver CHAI and an imaging spectrometer .

As most of large reflectors, CCAT-p's reflectors will be built by a set of panels that together produce the desired profile. As explained before, a high surface accuracy is required, a surface error measurement system for aligning the panels to achieve this precision. Millimeter wave holography has been chosen for this purpose, as it has been successful in similar applications [11],[12] and [13]. This technique derives surface errors at the reflectors from the measurement of the antenna diffraction pattern in amplitude and phase. Moreover, other antenna characteristics, as pointing and focusing, can be measured.

Applying holography techniques to this telescope, despite being a well known technique, present various challenges. Between them the election of the source location. An artificial source located at a distance of 300 m will be used, which is in the near-field of the telescope. Due to this, we require corrections to the standard procedure. The holography will be performed with a 295 GHz source. This frequency was chosen because it has direct relation on the accuracy needed in the holography. Similar applications were made in ALMA [14] and NANTEN2 [15] at  $\sim 100$  GHz achieving accuracy near  $20 \mu\text{m}$  RMS and we want almost three times better accuracy. Moreover, 295 GHz is a passive band [16] and has advantages in its performance. On the other hand, in its standard form, in which a single measurement is made on-axis, the derived errors will be the contributions of the two reflectors surfaces errors. For achieving the desired accuracy it is needed to separate each contribution, which in principle will be possible by making additional measurements in other positions of the focal plane [17].

This work focuses on making accurate simulations of the CCAT-p telescope holography, generating data on its behaviour at far and near field under different scenarios. This work also probes the feasibility of separating surface errors into each reflector contribution by measuring the diffraction pattern at different points of the focal plane.

### **1.0.1 Hypothesis**

By using millimeter wave holography and measuring the diffraction pattern of the CCAT-p telescope at different positions of the focal plane, it will be possible to separate the measured surface error into the contributions of each reflector surface error.

### **1.0.2 Objectives**

#### **General Objectives**

- 1)Generate simulation data about the holography for CCAT-p telescope under different scenarios.
- 2)Studying the feasibility of separating the measured surface error into the contributions of each reflector surface error.

#### **Specific Objectives**

- 1)Generate the following software simulations of the CCAT-p telescope:
  - Near-field at 300 m.
  - Far-field.
  - Surface errors at the reflectors.



-Make measurements at different points of the focal plane.

2) Simulations should have enough resolution to resolve each panel of the telescope.

3) Recover the illumination at the telescope's aperture by using software and the simulations data. With this, generate surface error maps for the study of errors at each reflector behaviour.

### **1.0.3 The structure of this thesis**

The rest of this thesis is organized in 4 chapters. In chapter 2, we will show a brief bibliographic review and theory revision of the concepts necessary to understand this work, with focus on the telescope geometry and holography. Chapter 3 shows the design parameters of the CCAT-p telescope and holography requirements and then they are applied into the simulations shown in chapter 4. In chapter 5, we show the results made by the analysis of simulations in chapter 4. Finally, in chapter 6 we summarize the obtained results and show the conclusions and future work.

# Chapter 2

## Bibliographic Review

We begin by reviewing the Crossed-Dragone optical design, followed by surface error considerations and finally present holography principles.

### 2.1 Crossed-Dragone Design

The design of the Crossed-Dragone (CD) multireflector antenna was presented by C.Dragone around 1978. It is an offset telescope which eliminates the cross-polarization and has circularly symmetric far-field pattern [9].

A parabolic reflector can generate a circularly symmetric pattern by centering it at the axis of an appropriate feed which also radiates a spherical wave with circular symmetry. Moreover, the parabolic antenna will have the same polarization as the feed. The problem with this configuration is that the feed will block part of the wave radiated by the reflector. This can be solved by offsetting the feed. However, this solution will cause asymmetry in the far field pattern and, in consequence, undesired cross-polarization. As shown in [9], as consequence of an equivalence principle in which a sequence of reflectors is always equivalent to a single reflector, if symmetry is to be preserved, the principal ray of the feed must coincide with the symmetry axis of this reflector. So, by combination of a number of confocal reflectors(ellipsoids, paraboloids or hyperboloids), this cross polarization can be eliminated and have a circularly symmetric far-field pattern.

The CD telescope uses this properties by using two reflectors, a primary reflector with paraboloid surface and a secondary reflector with hyperboloid surface. Another important feature of this telescope is its wide diffraction-limited field of view (DLFOV), obtained because of its low blockage geometry.

Behind, a brief summary of the geometry of the CD design based on [18] is presented and in figure 2.1 we show a scheme of the CD configuration. As mentioned before, it consists of a parabolic main reflector (MR) and a hyperbolic secondary sub reflector (SR), both with

elliptical rims. The CD geometry can be fully described by 20 design parameters, but only 5 of them need to be provided because from them the others can be determined.

**1)Main Reflector:** The main reflector has a parabolic surface and an elliptical rim. The parabolic reflector depends on the focal length  $F$  and can be described by

$$z = \frac{x^2 + y^2}{4F} - F. \quad (2.1)$$

Its elliptical rim is described by

$$\frac{x^2}{a^2} + \frac{y^2}{b^2} = 1, \quad (2.2)$$

where  $a$  is the semi-major axis and  $b$  is the semi-minor axis.

**2)Sub Reflector:** The sub reflector has a concave hyperbolic surface which depends on the parameters  $a$  and  $f$

$$z = -a\sqrt{1 + \frac{x^2 + y^2}{f^2 - a^2}} - f, \quad (2.3)$$

where  $f$  is half of the inter-focal distance and  $a$  is an hyperbola parameter.

The 20 parameters that describe the geometry of a CD telescope are shown in table 2.1 and figure 2.1, which are taken from the original C. Dragone paper [1]. In chapter 3 the CCAT-p specific design values are shown.

## 2.2 Surface error

Surface error or surface accuracy is the deviation of a surface from its ideal form, as shown in figure 2.2. The need for better angular resolution (minimum distance between distinguishable objects in an image) in image-forming devices has led to larger aperture telescopes and higher frequencies of operation. In fact, it depends directly of both parameters. In circular apertures this is expressed as

$$\theta = 1.22 \frac{\lambda}{D}, \quad (2.4)$$

where  $\theta$  is the angular resolution in radians,  $\lambda$  is the operation wavelength in meters and  $D$  is the diameter of the aperture. Because of this, it is common in radio astronomy and deep-space communications that reflectors may be very large and consequently they have to be constructed by a set of panels, instead of one big single surface. The panels that conform the final structure have to be calibrated so they form the right shape, for example, a parabolic surface. Each panel usually has a number of support points to the backup structure that allows the adjustment. On the other hand, high frequency (small wavelength) puts on its own challenge on the reflector construction, as diffraction will occur with smaller surface imperfections (comparable with the wavelength). Hence, large-aperture high-frequency operating antennas have very challenging demands on calibration accuracy and precision, which

**Table 2.1:** Crossed-Dragone telescope geometry parameters.

Parameter	Description
$D_m$	Diameter of the MR aperture.
$F$	Focal length of the MR.
$h$	Offset distance of the MR, i.e., distance between MR axis and aperture center.
$\theta_0$	Offset angle of the MR.
$\theta_U$	Offset angle of the top of the MR.
$\theta_L$	Offset angle of the bottom of the MR.
$e$	SR eccentricity.
$a$	SR parameter, distance between one of the vertex and axis of symmetry of an hyperbola.
$f$	SR parameter, half of the inter-focal distance of an hyperbola.
$C_{sr}$	Point expressed in the SR coordinate system defining the center of the SR elliptical aperture.
$\mathbb{D}_{sx}$	Major axis of the SR elliptical aperture taken parallel to the x axis of the SR coordinate system.
$\mathbb{D}_{sy}$	Major axis of the SR elliptical aperture taken parallel to the y axis of the SR coordinate system.
$\beta$	Angle between MR and SR axes.
$\theta_e$	Angle between the feed axis and the edge of the SR (taper angle of the feed).
$\theta_p$	Angle between the MR z axis and the feed z axis.
$\alpha$	Feed angle with respect to SR z axis.
$L_s$	Distance of the SR to the feed, following the central ray.
$L_m$	Distance between the SR and MR following the central ray.
$d_{f-mr}$	Minimum vertical distance between the feed and the MR edges.
$d_{sr-mr}$	Minimum vertical distance between the SR edges and the MR edges.



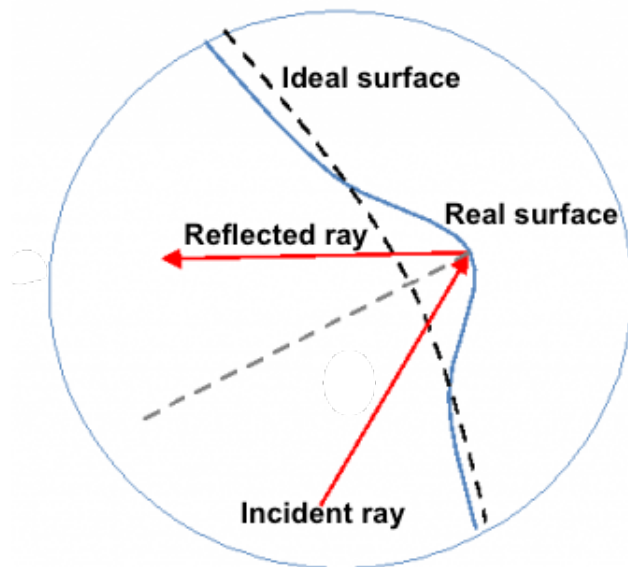


**Figure 2.2:** Surface error.

scopes [22]. The setting of the panels at such accuracy needs reflector metrology techniques, which includes the use of theodolites, photogrammetry and holography. Measurements with theodolites has taken 6 weeks of down time to achieve a 0.5 mm RMS accuracy in ALMA [23]. Photogrammetry has also been used in ALMA antennas achieving 40–30  $\mu\text{m}$  accuracy [24]. One of the most precise and versatile technique is millimeter-wave holography which has been used at IRAM 30 m millimeter telescope [25], NASA Deep Space Network Antennas (DSN) [8], ALMA [11] and APEX [13] among many others.

## 2.3 Holography

Millimeter-wave holography is a technique used to measure surface errors in millimeter and submillimeter reflectors, as well as panel alignment, antenna aperture illumination, directivity and gravity deformation effects [23]. It is the less time-consuming method and has very good accuracy. This method utilizes the Fourier-transform relation between the field distribution in the aperture plane and the far-field diffraction pattern (if near-field is used, a correction is needed), providing a map of the surface error distribution across the aperture, as well as the focusing or pointing errors. It allows to derive the adjustment in each panel position to achieve the needed reflector shape.

The holography technique needs to measure the complex beam pattern (far-field or near-field) in two dimensions, i.e the amplitude and phase response. The amplitude measurement will give the illumination distribution at the aperture while the phase measurement the information about misalignments in the panels. The mathematic principle of this Fourier transform relation can be seen in more details in [14], here we describe briefly the procedure. Referring to figure 2.3, the radiation function  $f(x, y, z)$  at a point  $P$  in space is related with

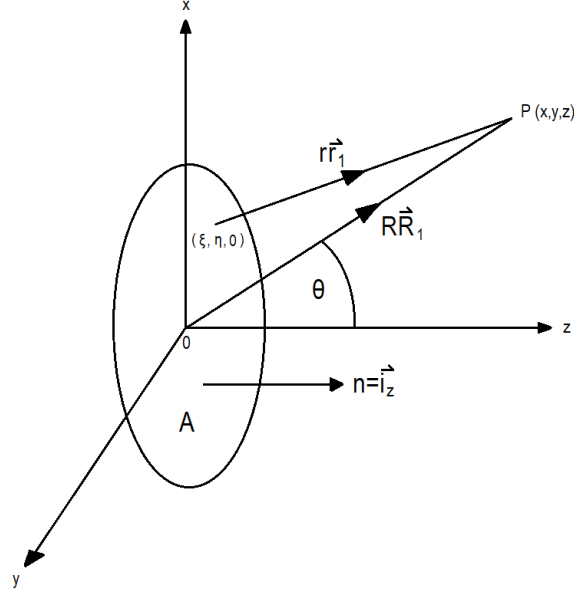


**Figure 2.3:** Aperture and  $P(x,y)$  coordinate system.

the field distribution  $F(\xi, \eta)$  over the aperture as follows

$$f(x, y, z) = \frac{1}{4\pi} \int F(\xi, \eta) \frac{e^{-ikr}}{r} \left[ (ik + \frac{1}{r} \vec{i}_z \cdot \vec{r}_1 + ik \vec{i}_z \cdot \vec{s}) \right] d\xi d\eta, \quad (2.6)$$

where  $k = 2\pi/\lambda$ ,  $s$  is the propagation vector of the wave field in the aperture, and  $\vec{r}_1$  and  $\vec{i}_z$  are vectors. For this equation it is assumed that the aperture is large compared to the wavelength.

### 2.3.1 Far and near field

The diffraction field surrounding an aperture can be divided into three zones, the reactive near-field, the near-field (Fresnel diffraction) and the far-field (Fraunhofer diffraction). The reactive near-field (which is not studied in this work) does not allow any approximation, but near and far field conditions yields simplifications to equation 2.6. For example, considering that the point  $P$  is far from the aperture (in terms of wavelengths) equation 2.6 gets simplified to

$$f(x, y, z) = \frac{i}{2\lambda R} \int F(\xi, \eta) [\cos(\theta + 1)] e^{ikr} d\xi d\eta. \quad (2.7)$$

This equation can be used at the far-field and at the near-field if  $r$  is at least several aperture diameters large.

#### Far-field (Fraunhofer diffraction)

In the case of far-field, where  $R$  tends to infinity,  $\vec{r}_1$  and  $\vec{R}_1$  may be considered as parallel. Additionally, considering that for high-gain antenna most of the energy is concentrated

in a small angular region ( $\theta$ ), we apply the Fourier transform to equation 2.7. First,  $r$  (distance from any point in the aperture to the field point  $P$ ) is approximated to

$$r = R - u\xi + v\eta. \quad (2.8)$$

Then, we obtain

$$F(\xi, \eta) = \frac{1}{4\pi} \frac{e^{ikr}}{R} \int f(u, v) e^{ik(u\xi + v\eta)} du dv. \quad (2.9)$$

Here  $u$  and  $v$  are the direction cosines of the field point defined as

$$x = R \sin(\theta) \cos(\phi) = Ru, \quad (2.10)$$

$$y = R \sin(\theta) \sin(\phi) = Rv, \quad (2.11)$$

$$z = R \cos(\theta) = R\sqrt{(1 - u^2 - v^2)}. \quad (2.12)$$

Then, the relation in equation 2.9 shows that if the entire far-field pattern  $f(u, v)$  amplitude and phase is measured, a full description of the aperture field distribution (also amplitude and phase) can be obtained. textbf

Near-field (Fresnel diffraction)

In the near-field case a correction to equation 2.9 is required, mainly because the distance  $r$  cannot be approximated as in 2.8 and higher order terms have to be considered. This leads to the following near-field relation,

$$F(\xi, \eta) = \frac{i}{\lambda} \frac{e^{-ikr}}{R} \exp\{-ik\delta p_1(\xi, \eta)\} \int f(u, v) \exp\{ik(u\xi + v\eta)\} e^{-ik\varepsilon} du dv, \quad (2.13)$$

where  $r$  is given by

$$r \approx R - u\xi + v\eta + \delta p_1(\xi, \eta) + \varepsilon. \quad (2.14)$$

In this expression  $\delta p_1$  and  $\varepsilon$  are

$$\delta p_1(\xi, \eta) = \frac{\xi^2 + \eta^2}{2R} - \frac{(\xi^2 + \eta^2)^2}{8R^3}, \quad (2.15)$$

$$\varepsilon = -\frac{(u\xi + v\eta)^2}{2R} + \frac{(\xi^2 + \eta^2)(u\xi + v\eta)}{2R^2}. \quad (2.16)$$

In [20] there is an analysis of how this terms  $\delta p_1$  and  $\varepsilon$  affect the equation 2.13.

### 2.3.2 Sampling and resolution

Measuring the entire radiation pattern could be very difficult. It has been shown in [8] that if the radiation pattern is measured over a sufficiently large area, the field distribution at the



aperture can be recovered with a certain resolution, given by the Nyquist theorem. Here we summarize this procedure.

First, we define the half power beamwidth of an aperture (HPBW),

$$HPBW[^\circ] \approx \frac{\lambda}{D}, \quad (2.17)$$

where  $\lambda$  is the wavelength and  $D$  is the diameter of the aperture. This HPBW is approximately the angular resolution of the antenna (minimum distance between distinguishable objects in an image) and, consequently, it puts a bound on the maximum spacial frequency  $B$  that the antenna can measure. The antenna cannot distinguish between objects with higher spatial frequency than  $B$ ,

$$B = \frac{D}{\lambda}. \quad (2.18)$$

Following the Nyquist-Shannon sampling theorem, the sampling frequency  $f_s$  should be at least  $2B$ , so that the distance between samples has to be less than the HPBW.

Let us suppose that we measure the radiation pattern on a 2D square grid of a number  $N$  of points, each one with a spacing  $u$  less than the HPBW,

$$\Delta u = k \frac{\lambda}{D}, \quad (2.19)$$

where  $0.5 < k < 1.0$  is a constant. Then, the length  $L$  of the grid can be expressed as

$$L = Nk \frac{\lambda}{D}. \quad (2.20)$$

If we consider that this as a rectangular pulse of length  $L$ , then the spatial Fourier transform of this pulse will be

$$\frac{\sin(\pi Lx)}{\pi Lx}. \quad (2.21)$$

This function has its zeros at entire multiples of  $x = \frac{1}{L}$  so the full null width of this function is  $2 \times \frac{1}{L}$ . If we define the spatial resolution to be at the 50-percent width, then the resolution  $\delta$  obtained at the aperture will be

$$\delta = \frac{\lambda}{L}, \quad (2.22)$$

where  $L$  is in radians and  $\delta$  and  $\lambda$  are in meters.

### 2.3.3 Holography Accuracy

As showed in [8], the accuracy obtained in the final maps derived from holography can be measured as the standard deviation in recovering the mean position of a resolution cell. The accuracy  $\sigma$  can be calculated by

$$\sigma \cong 0.082 \frac{\lambda D}{\delta SNR}, \quad (2.23)$$

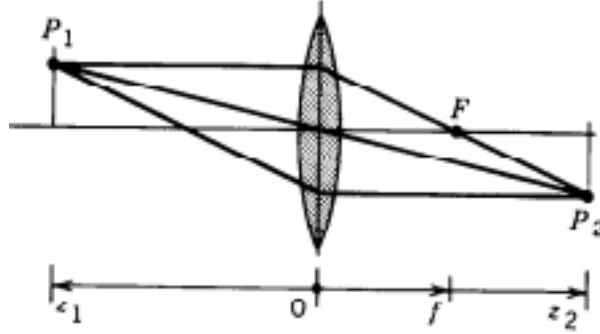


**Figure 2.4:** Imaging equation [31].

where  $\lambda$  is the holography wavelength,  $D$  is the reflector diameter,  $\delta$  is the spatial resolution in the aperture plane and SNR is the beam peak voltage SNR in the test (antenna) channel. For a uniform illumination, accuracy stays relatively constant along the reflectors. For non uniform illumination, it varies with the amplitude taper, having better accuracy at the center of the dish and decreasing towards the edges [8].

## 2.4 Miscellaneous

### 2.4.1 Imaging equation

In the case of CCAT-p, the source will be located at 300 m, which is at the near-field of the telescope (this will be explained with more details at chapter 3). The imaging equation states that when an imaged object is at an infinite distance of a lens, it will form at a distance corresponding to the focal length  $f$ . This is not the case for the holography source of the CCAT-p, so we have to recalculate where the image will form.

Referring to figure 2.4, in the context of ray optics, if an imaged object is at a distance  $z_1$  to a lens, the distance  $z_2$  between the image formed and the lens are related by

$$\frac{1}{z_1} + \frac{1}{z_2} = \frac{1}{f}, \quad (2.24)$$

where  $f$  is the focal length of the lens. If the object is at a infinite distance  $z_1$ , we can deduce that the image will form at a distance  $z_2 = f$ . Otherwise, if is not at infinity, the location of the image changes.

## 2.5 Summary

In this chapter we presented the Crossed-Dragnone optical design, an offset telescope which eliminates the cross polarization and has wide DLFOV. Also, we gave the basic parameters

for defining this design. The CCAT-p telescope has this geometry. We defined surface error and its importance for the telescope performance, particularly, in the efficiency of the antennas. Holography principles were explained and its calculation at near and far field. Additionally, we reviewed the procedure for calculating the resolution and sampling needed for the holography, as well as its accuracy. Finally we showed the imaging equation, needed for calculating where an image will form depending on the distance from the source to the imaging system.

# Chapter 3

## Design Parameters and Requirements

In this chapter we show first the design parameters of CCAT-p. Then, we show the holography requirements and simulation parameters.

### 3.1 CCAT-p optical design

In chapter 2 the geometry of CD telescopes, their basic parameters and characteristics were described. Here we present the specific design values of CCAT-p.

CD telescopes have a large diffraction limited field of view (DLFOV) with excellent polarization fidelity. They have been used for CMB measurements in two small aperture telescopes [26] [27] and have been proposed as good alternative for NASA's Inflation Probe [28]. However, all of these designs have small focal radius and place detectors directly on the focus of the telescope, which implies a lot of spillover after the primary and second mirror [6].

The first conceptual design of the CCAT-p is presented by M. Niemack design in [6]. It describes various CD telescopes with large aperture and focal radius, eliminating the previously mentioned problem. The telescopes studied by Niemack were two 6-m telescopes designs, which give sufficient throughput to achieve 10 times faster mapping speed than upcoming instruments and the necessary resolution for CMB survey. Niemack's design is based on [18].

The actual production design has been developed by R. Hills design [29], which follows a 3:4:5 proportion. The reflectors of a classic CD telescope have conic surfaces (parabolic and hyperbolic for the CCAT-p), but for coma correction they were modified and defined with polynomial equations [30]. In this thesis we will work with the original conical surfaces. In table 3.1 and figure 3.1 we present some of the parameters listed in table 2.1 of the actual CCAT-P design, along with other parameters provided by the designers that could be useful.

**Table 3.1:** CCAT-p optical design parameters.

Parameter	Description
$D_m$	6000 mm
$F$	28800 mm
$h$	28800 mm
$\theta_0$	53.130 deg
$e$	2.236
$a$	9000 mm
$f$	20124.6
$\beta$	63.435 deg
$\theta_e$	11.894 deg
$\theta_p$	90 deg
$\alpha$	26.565 deg
$L_s$	12000 mm
$L_m$	6000 mm
$L_p$ (Distance SR To prime focus on axis)	6000 mm
$K$ (SR constant conic)	-5
$R$ (SR radius of curvature)	36000 mm
$m$ (magnification of SR on axis)	0.382
$M$ (actual magnification)	0.4
$f_{eff}$ (effective focal length)	14400 mm
$inc_p$ (MR chief ray angle of incidence)	26.565 deg
$inc_s$ (SR chief ray angle of incidence)	18.435 deg
$f - ratio$ (secondary f-ratio )	26.565 deg

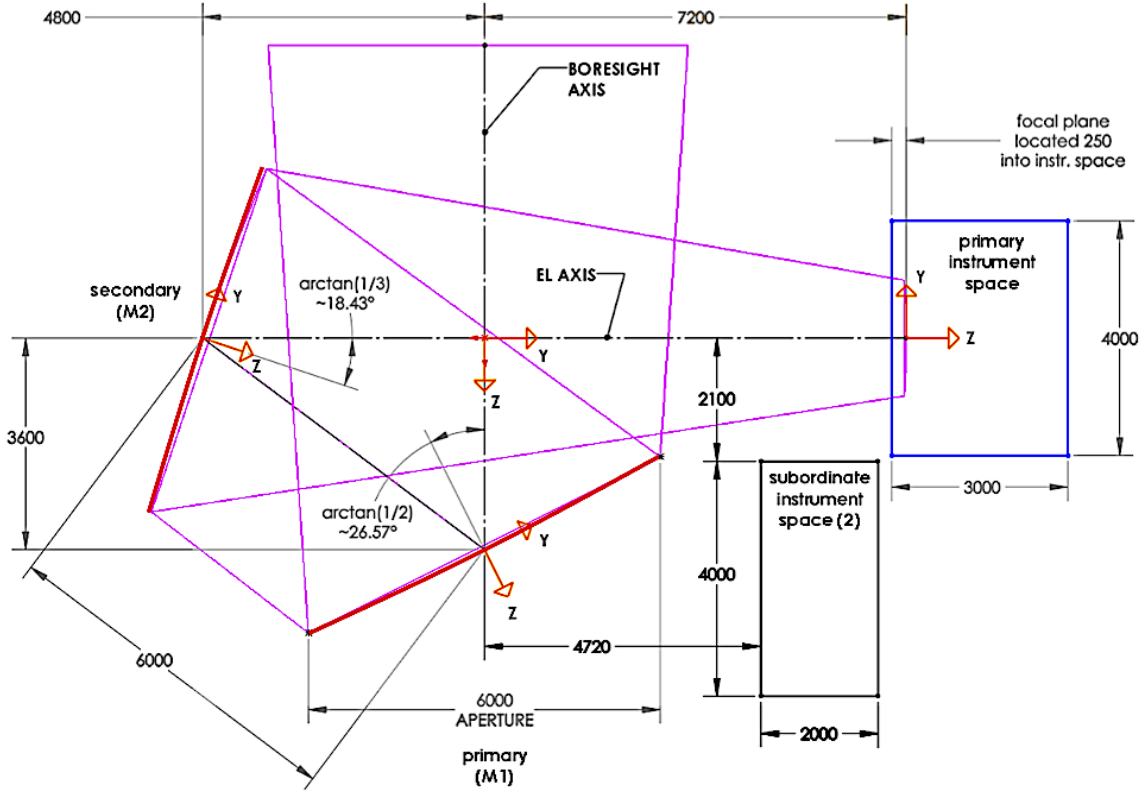


Figure 3.1: CCAT-p optical design [30]. All lengths are in mm.

## 3.2 Holography Requirements

Millimeter-wave holography was chosen as the technique for measuring surface errors at the telescope reflectors of CCAT-p because it has proven to be successful in other similar projects [11]. The theory behind holography was explained in Chapter 2.

Implementing classical holography for this telescope has the issue that the derived surface error will be the sum of the contributions of each reflector surface. To be able to correct each reflector, it is proposed to take measurements in different positions of the focal plane. Here we describe the CCAT-p holography requirements and parameters, they are explained in more detail in [17].

### 3.2.1 Operating Frequency

Traditional holography made at ALMA [14], APEX [13] and NANTEN2 [15] operates at 100 GHz, reaching a surface accuracy of about 20  $\mu\text{m}$  RMS and a measurement accuracy of 5  $\mu\text{m}$  RMS. Since we want to achieve almost three times better accuracy, 7 and 3  $\mu\text{m}$  RMS respectively, a 295 GHz source has been selected. As described in Chapter 2, the resolution obtained at the aperture is proportional to the wavelength and the holography accuracy. Moreover, it is an advantage to use the highest possible frequency. Since a phase error produced in the wave front, for example due to errors in the feed horn, will translate into a

smaller error in the aperture. In the downside, at higher frequencies it will be more difficult to obtain commercial components, attenuation in the atmosphere will turn more significant and there are passive bands that have to be avoided [16]). The 295 GHz frequency meets with all this requirements.

### 3.2.2 General Requirements

**1) Accuracy:** The goal for the surface of the telescope is  $10\text{--}7\ \mu\text{m}$  RMS. Therefore, an holography of  $3\ \mu\text{m}$  RMS has been set to take into account possible random and systematic errors.

**2) Spatial resolution:** As shown in section 2.3.3, the spatial resolution obtained at the aperture is inversely proportional to the angular size of the map made from the radiation pattern. The surface panels will have a length of  $600\times 675\ \text{mm}$  (projected on the aperture), each one with 5 vertical adjustment points. Therefore, a spatial resolution at the aperture of  $100\ \text{mm}$  is chosen to be able to resolve each panel along with their adjusters.

**3) Time to complete a measurement:** The measurements need to be taken in a time interval short enough to allow repeated measurements without changing the environmental conditions. An upper limit of 20 minutes has been set. However, the requirement is that the holography system should be able to take a full resolution map in 10 minutes. The telescope drives should allow this requirement.

**4) Make measurements from multiple positions in the focal plane:** Because of the large DLFOV, being able to make measurements at different positions of the focal plane is necessary. It has been set a requirement of  $\sim 5$  well separated different positions at the focal plane, at about  $1\ \text{m}$  off-axis. This will be crucial for separating errors coming from each of the apertures.

**5) No radio frequency interference:** The holography measurement antenna will be very close to ALMA and another telescopes, so it has to satisfy the ITU requirements. Since the 295 GHz is a passive band [16], the signals used for holography should not be emitted in the direction of the other facilities.

### 3.2.3 Taking Data

As shown in chapter 2, the length of the beam-pattern map is inversely proportional to the resolution that will be obtained at the aperture plane. The radiation pattern needs to be sampled at a spacing of about  $0.8\lambda/D$ , which for a frequency of 295 GHz ( $\lambda = 0.001\ \text{m}$ ) and an aperture of  $D = 6\ \text{m}$  gives  $\theta = 28\ \text{arcsec}$ . Then, if the length of the map  $L$  is  $2520\ \text{arcsec}$  ( $0.7^\circ$ ), the resolution at the aperture will be  $\delta = 83\ \text{mm}$  (spatial resolution which accomplishes the requirement mentioned in section 3.2.2). The number  $N$  of samples then

can be chosen as  $N=91$ . In this work we have used  $N=273$  points for the simulations, but they can be easily transformed in  $N=91$  points by taking an average every 3 pixels.

For taking the holography measurements there are two points that need special care. They are that the timing of the sampling must be well-synchronized with the scanning and that the telescope pointing is sufficiently accurate in spite of the motion. Two options have been considered for the data-taking, a unidirectional rectangular raster scan and a double-circle pattern.

### 3.2.4 Source Location

Only ground-based sources for holography have been considered. Astronomical sources are too weak to comply with the system requirements. Using distant locations is not very practical too because it will be difficult to access to the source and the atmosphere will produce undesirable large attenuation and fluctuations reducing the measurement accuracy. There are two suitable options. One of this is the TAO building, which is  $\sim 200$  m away with an elevation angle of  $\sim 10^\circ$  (which will imply a shift of  $\sim 1.1$  m in the focus position by using the imaging equation 2.24). The second option is in the road that goes from CCAT-p to the TAO building at  $\sim 300$  m from the telescope and at an elevation of  $\sim 3.5^\circ$ . The later location implies a shift of 0.75 m of the focus position. The preferred location is, therefore, the  $\sim 300$  m on the road location (because of the smaller shift in the focus position). The receiver will be located 0.5 m behind the nominal focal plane instead of 0.75 m because it will provide a better dynamic range. These locations are much more practical, as the access to the source will be easy and the atmospheric effects will be small. However, they are both in the near-field of the telescope, so corrections will be needed. A map of the source location is shown in figure 3.2. If the TAO location is the selected it might require the mapping of a larger area taking more time.

Other considerations are that the source will need to be raised at least 1.5 m above the ground to avoid reflections. It also needs to be well supported for wind protection and it has to be battery powered. The signal for holography is planned to be emitted in a narrow beam (less than  $3^\circ$  wide) directed about  $25^\circ$  degrees east of north (for avoiding interference with other facilities).

## 3.3 Summary

In this chapter we gave the design parameters for the CCAT-p telescope and the holography requirements. This parameters are used for the simulations and analysis made in this thesis.



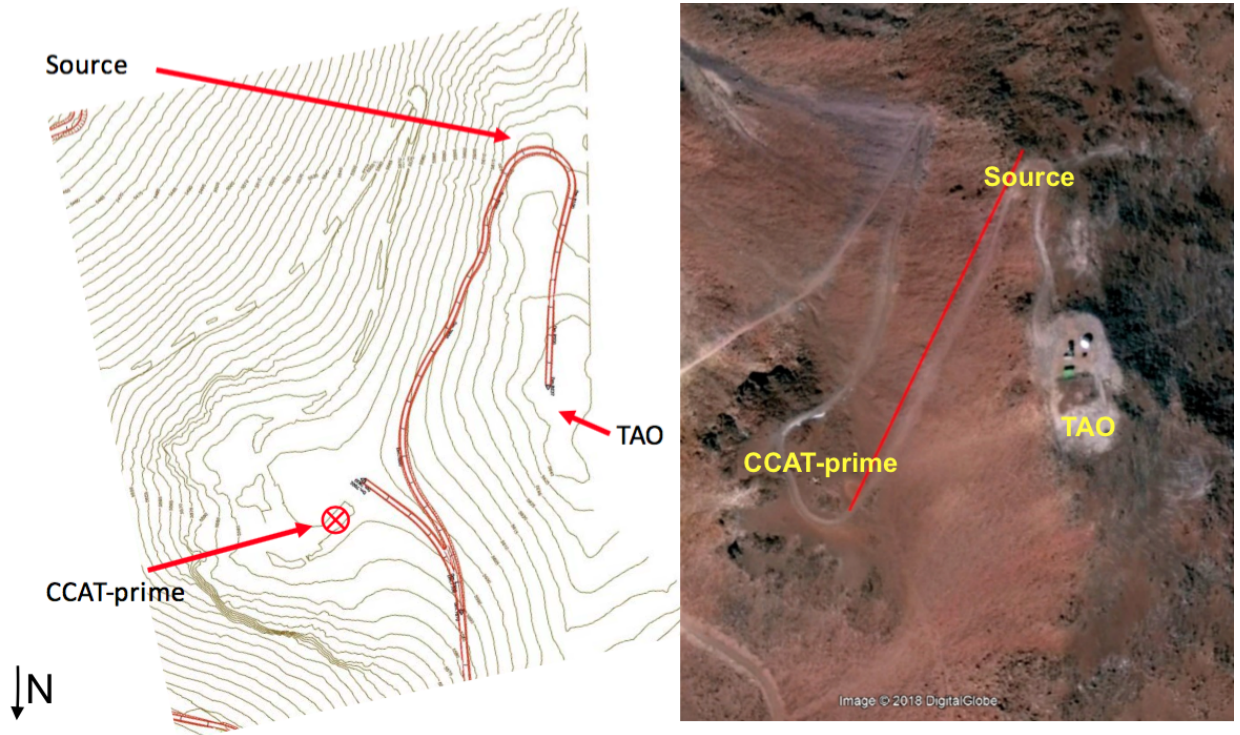


**Figure 3.2:** Possible location of the holography source.

# Chapter 4

## Simulations

The holography technique will be implemented for achieving the surface accuracy goal of  $10\text{--}7\ \mu\text{m}$  RMS for the CCAT-p telescope. This will be realized with a 295 GHz artificial source located at 300 m in the near-field. As the telescope has two 6-meter reflectors, the holography measurements will give the sum of both surface errors contributions. To be able to separate the total error into each reflectors errors, we will take measurements in four positions of the focal plane.

For studying how CCAT-p holography will behave under the indicated conditions, simulations are essential. It is of special interest simulating how the diffraction pattern of the source looks at the 300-m near-field location with a focal plane 0.5 m behind the nominal focal plane. Furthermore, for proving the wide field of view (FOV) and the feasibility of separating errors contributions of each reflector, far-field simulations are required.

### 4.1 CCAT-P Simulations under different scenarios

In an early stage of the project we started with simulations of the telescope using Zemax OpticStudio, modeling the optics and using ray tracing algorithms. Zemax OpticStudio is an optical design program that is used to design and analyze imaging systems, it uses ray-tracing modelling [32]. However, since we wanted to simulate diffraction patterns of the telescope, we decided to change to GRASP (General Reflector Antenna Software Package) developed by TICRA [33]. GRASP is a software specialized in reflector antennas, in which is easy to define dual reflector systems with axial displacement. It uses an advanced physical optics (PO) method and allows near and far field analysis. Physical optics gives an approximation of the surface currents for perfectly conducting and large (in terms of wavelength) scatterers [34]. This approximation is good for studying diffraction, interference and polarization effects. In summary, GRASP software allows us to easily model the geometry of CCAT-p telescope, make accurate simulations with the resolution that we need and make analysis in

near and far field.

In the rest of the chapter we show the simulations of CCAT-p holography made in GRASP software. For these simulations the telescope was modeled following the parameters shown on table 3.1 and the scheme of figure 3.1. The feed in the software emits a Gaussian beam at 295 GHz (the frequency chosen for the holography) and has a taper of  $-8$  dB for obtaining a good illumination over the edges of the reflectors.

The amplitude and phase of the electric field was recorded at the far-field and the near-field (at 300 m). A spherical elevation over azimuth grid of  $273 \times 273$  points centered at the aperture was used. The aperture plane is chosen as the plane located on the intersection of the azimuth and elevation axes. The angular length of the grid was  $0.7^\circ \times 0.7^\circ$ , calculated for reaching the desired resolution. The accuracy of the simulations is  $-40$  dB, meaning that each calculated current causes a pattern change less than the specified field accuracy.

We have simulated three different scenarios for the reflectors surfaces, with the purpose of studying how errors behave at each reflector. The details of each scenario are shown in sections 4.1, 4.2 and 4.3. This scenarios are:

- **First scenario:** We simulate the ideal telescope, i.e. reflectors with perfect surfaces.
- **Second scenario:** We simulate the telescope with a well defined error placed at the main reflector surface (MR).
- **Third scenario:** We simulate the telescope with a well defined error placed at the secondary reflector (SR) surface.

As mentioned previously, one of the main issues of doing holography for the CCAT-p is the separation of errors at each surface. For the study of this problem we have taken measurements of the electric field with the feed located at four positions of the focal plane shown in figure 4.1. This positions are defined as:

**Feed positions:**

- a) Feed on-axis.
- b) Feed off-axis by 50 cm in the x axis.
- c) Feed off-axis by 50 cm in  $+120^\circ$  from x axis.
- d) Feed off-axis by 50cm in  $-120^\circ$  from x axis.

Taking into account this, we make simulations for each one of the three scenarios and take measurements with the feed at the four positions (a), b), c) and d)). Additionally, each simulations is made at the near and at the far field. This gives a total of 24 simulations, 8 for each scenario.

In this chapter, we show the most relevant results of each scenario, showing the amplitude and phase of the diffraction pattern for each case as it is necessary for the holography analysis. In this work, we focus on far-field simulations, because they are used in chapter 5 for the analysis of the errors at each reflector. The patterns shown where plotted with Python software using the data obtained with GRASP, they are all normalized and in dB. The model of the telescope, simulated by GRASP, is shown below on figure 4.2.

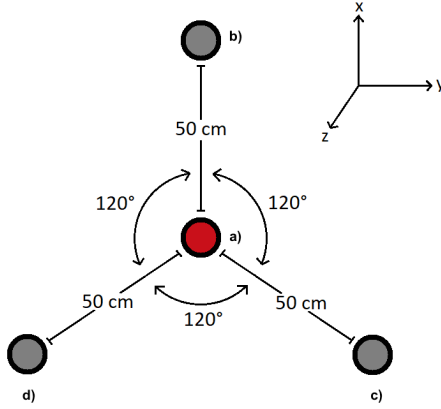


**Figure 4.1:** Four measuring positions at the focal plane.

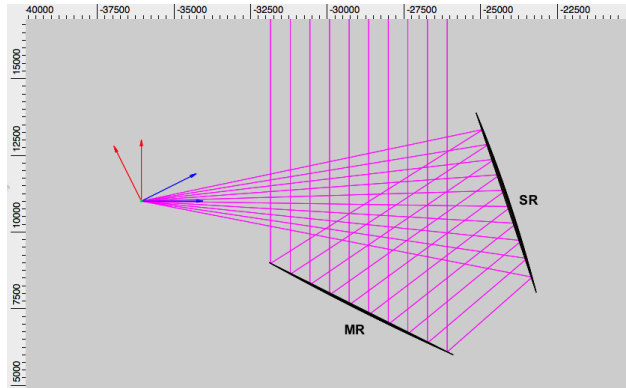


**Figure 4.2:** CCAT-p model on GRASP software. Blue arrow is the z axis and red arrow is the x axis (scale is in meters).

### 4.1.1 First scenario: Ideal surface CCAT-p simulations

The first scenario simulates ideal surfaces for the MR and SR. Eight different simulations were made, one for each of the four positions of the feed for the far-field and for the near-field. Here we show the Far-field simulations and the near-field simulation with the feed on-axis, 50 cm behind the focal plane.

#### Far-field simulations:

The ideal behavior of the telescope is shown on figure 4.3. We show the obtained diffraction pattern of the CCAT-p telescope, in amplitude and phase. First, in Figure 4.3a, the amplitude of the co-polar electric field ( $E_{co}$ ) is shown in dB and normalized and in figure 4.3b its phase in degrees. In Figure 4.3c the amplitude of the cross-polar electric field ( $E_{cx}$ ) is shown.

The Crossed-Dragone properties mentioned on section 2.1 are clearly demonstrated in figure 4.3. It can be seen in Figure 4.3a that the pattern is circularly symmetric, and that the maximum peak is achieved at the center of the focal plane, also figure 4.3c shows that the

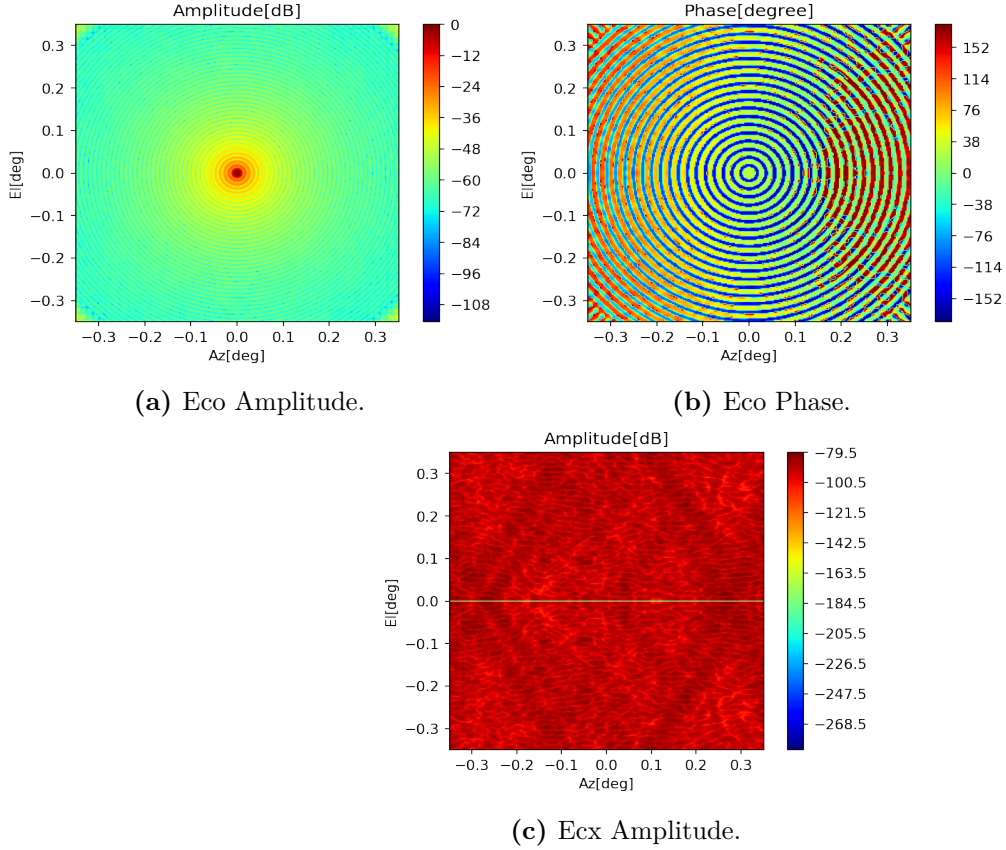


**Figure 4.3:** Far-field diffraction pattern of the CCAT-p telescope. We show the polar and cross polar electric field obtained by simulations.

cross polarization is very low.

Now we show the ideal case but with the feed off-axis, as we mentioned before, there are 4 positions for the feed considered. First in figure 4.4 we show the amplitude of the three off-axis cases b), c) and d) then in figure 4.5 we show the phase of each one of them.

The figures 4.4 and 4.5 shows how the far-field pattern is deformed in amplitude and phase by the change in the feed position, losing the circular symmetry. The maximum amplitude of the field moves from the center of the feed, to a new position determined by the feed location and the antenna scale factor (scale factor=  $0,00397^\circ/\text{mm}$ ).

### Near-field simulations:

As explained before, the source will be at 300 m from the telescope and we will measure 50 cm behind the nominal focal plane. In figure 4.6 the results for the on-axis feed are shown. The field pattern in figure 4.6a is circularly symmetric as expected and the amplitude has more homogeneous variations.

For the other positions of the feed, we only show the amplitude of the patterns in figure 4.7. It can be seen in figure 4.7 that the change of position of the feed changes the location

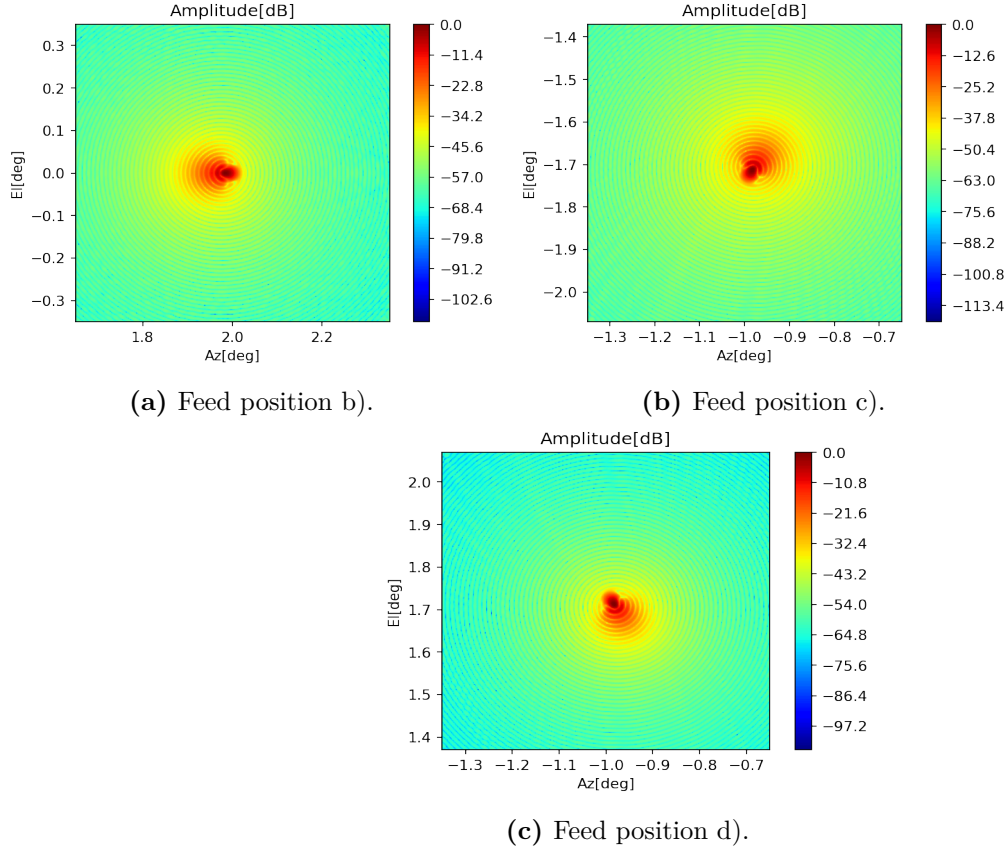


**Figure 4.4:** Electric field diffraction pattern of the CCAT-p telescope with the feed located at three off-axis positions. Simulations made at the far-field with ideal surfaces.

of the maximum amplitude of the pattern and that the circular symmetry is lost. If we compare this figure with the far-field case (figure 4.4) it can be observed that the location of the center of the pattern moves to the same location on both cases (far-field and near-field) and the orientation of the pattern turns in the same direction. This is as expected because it is the same pattern measured at different distances (at infinity and at 300 m respectively).

#### 4.1.2 Second scenario: Error at MR surface

The second scenario simulates a perfect surface for the SR and a surface with error for the MR. The error at the MR was simulated by a bi-dimensional Gaussian bump of width 60 cm (standard deviation of 30 cm) and height of 50  $\mu\text{m}$  (mean of 50  $\mu\text{m}$ ) located at  $(x,y)=(-1\text{m},-1\text{m})$  viewed from the center of the MR. This error was chosen as it is similar to a panel been lifted of the surface by 50  $\mu\text{m}$ . Again eight simulations where made for this scenario. In figure 4.8 we can see the location of the introduced error.



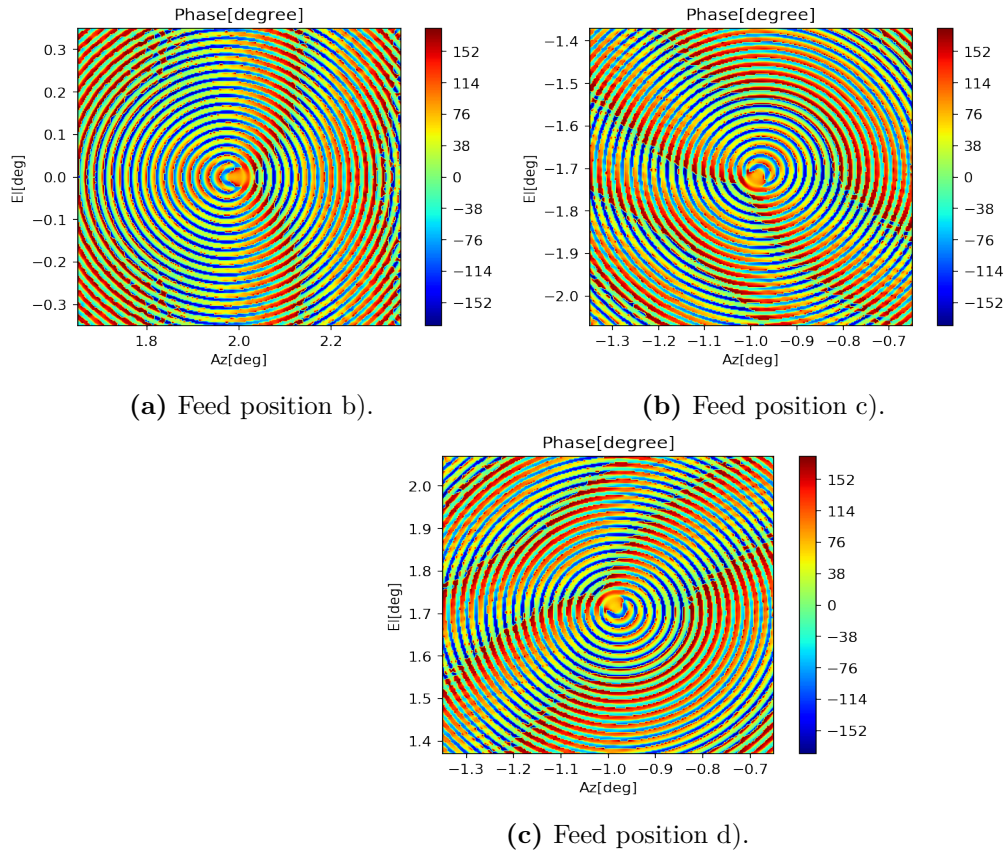


**Figure 4.5:** Phase of the electric field obtained for the three off-axis feed positions.

## Far-field simulations

Figure 4.9 shows the pattern obtained for this scenario with the feed on-axis. The patterns for the other positions of the feed change similarly than in the ideal case showed in figure 4.4 (surface without errors), but adding the error distortion to each pattern, so they won't be displayed in here. Comparing Figure 4.9 with Figure ??, it can be seen that the amplitude of the field is distorted when adding the Gaussian bump, being this effect more notorious near the center of the pattern, the field hasn't got circular symmetry anymore. The phase information also changes and loses its symmetry.

## Near-field simulations

Figure 4.10 shows the near-field pattern obtained when added an error at surface of MR. We only show the feed on-axis case because the others are a combination between figure 4.7 and figure 4.10. We observe in 4.10 how the symmetry is lost and that a perturbation appears in the upper right side of the pattern due to the error introduced.

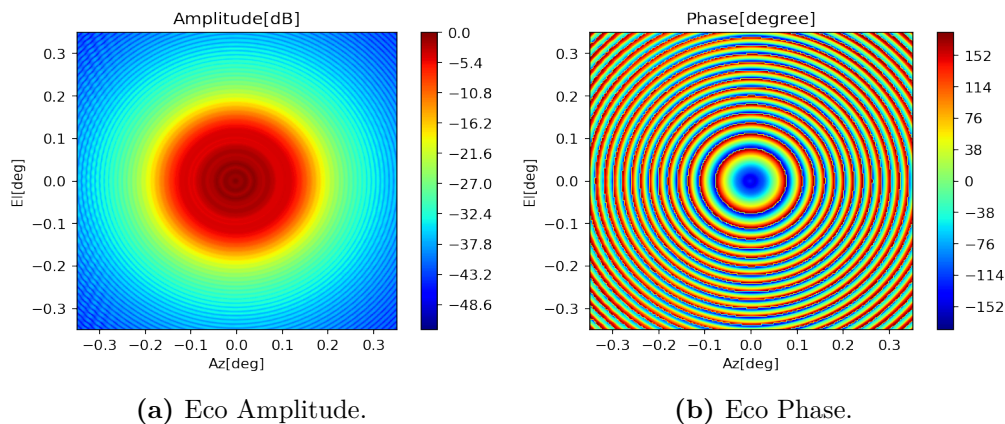


**Figure 4.6:** Near-field diffraction pattern for the telescope simulated with ideal surfaces.

### 4.1.3 Third scenario: Error at SR surface

The third scenario simulates perfect surface for the MR and a surface with errors for the SR. The error introduced at the SR was a Gaussian bump of width 30cm (standard deviation of 15cm) and height of 50  $\mu\text{m}$  (mean of 50  $\mu\text{m}$ ) located at  $(x,y)=(-1\text{m},1\text{m})$  viewed from the center of the SR. The previously mentioned eight simulations were made for this scenario. In figure 4.11 we can see the location of the error introduced.

#### Far-field simulations

Again we show the amplitude of the pattern in figure 4.12 with the feed on-axis, as patterns with the other positions of the feed are analogous to figure 4.4 but with deformations caused by the error.

Again the pattern changes in amplitude and phase because of the error at SR, losing its circular symmetry.

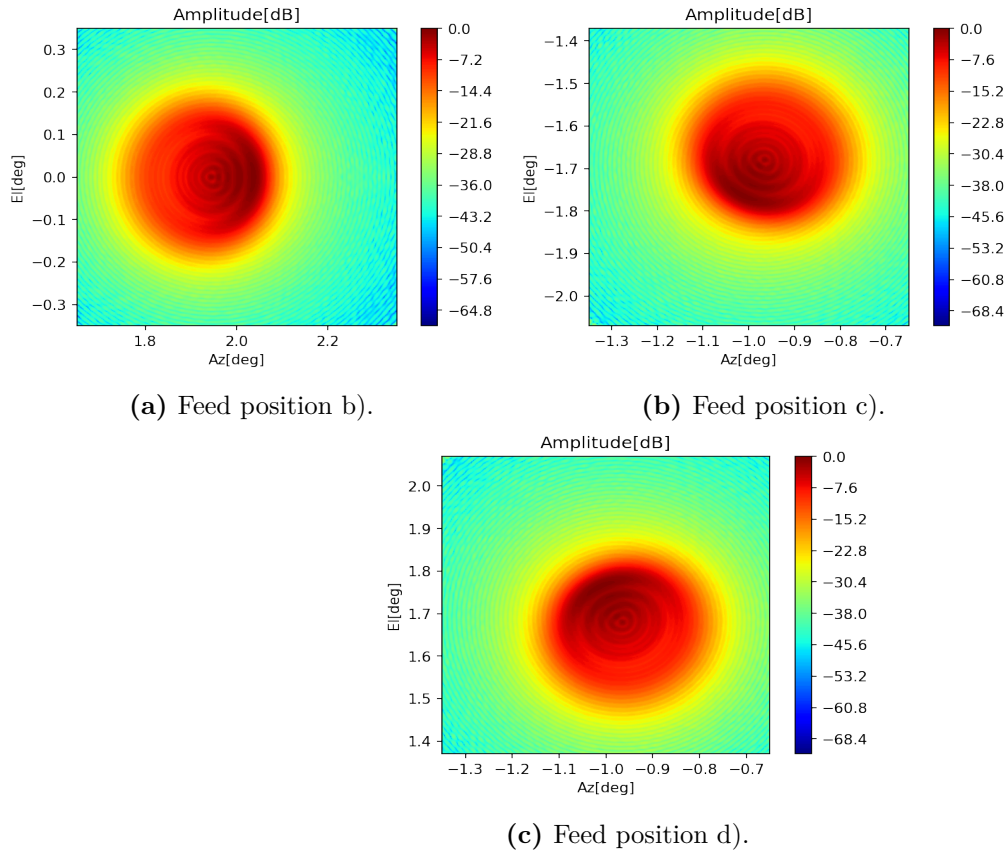
#### Near-field simulations

Figure 4.13 shows how the near-field pattern looks when added an error at surface of the SR. As previously, we are only going to show the feed on-axis case because the others are a combination between figure 4.7 and figure 4.13. We can see in 4.13 how the symmetry is lost and that again a perturbation can be observed in the upper left side of the pattern.

## 4.2 Conclusions

Introducing errors at the surfaces of the reflectors of the CCAT-p telescope causes changes in the obtained diffraction pattern, in amplitude and phase. Also, changing the position of





**Figure 4.7:** Near-field diffraction patterns for the CCAT-p telescope with ideal surfaces. We show the patterns obtained for three off-axis positions of the feed.

the feed causes differences between the patterns, causing loss of circular symmetry. We could observe that in the near-field the pattern behaves differently than in the far-field.

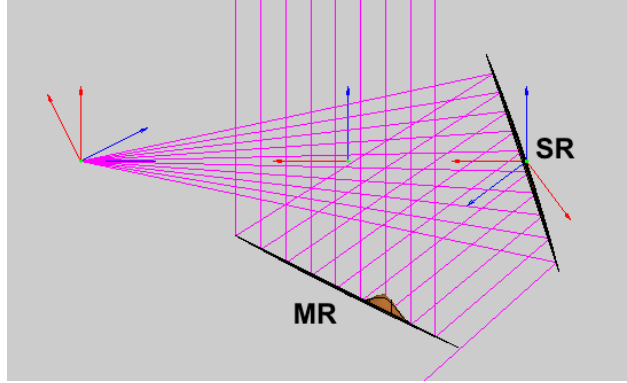


**Figure 4.8:** Location of surface error at the MR (the error is not in scale).

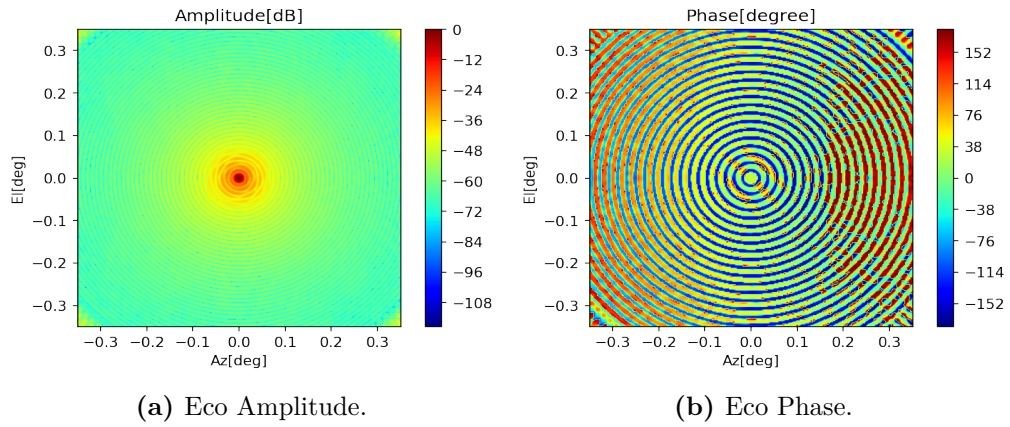


**Figure 4.9:** Electric diffraction pattern of the CCAT-p telescope with errors at the MR surface. Far-field simulation.

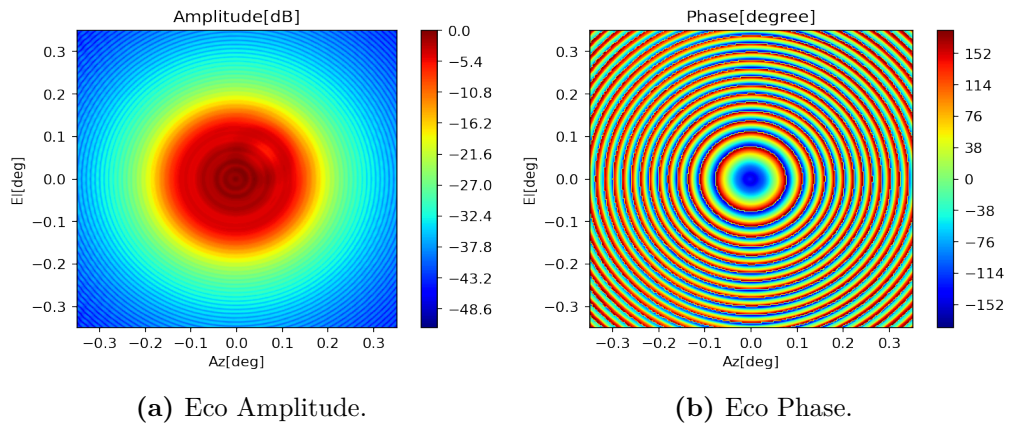


**Figure 4.10:** Near-field diffraction pattern of the CCAT-p telescope with errors at the MR surface.

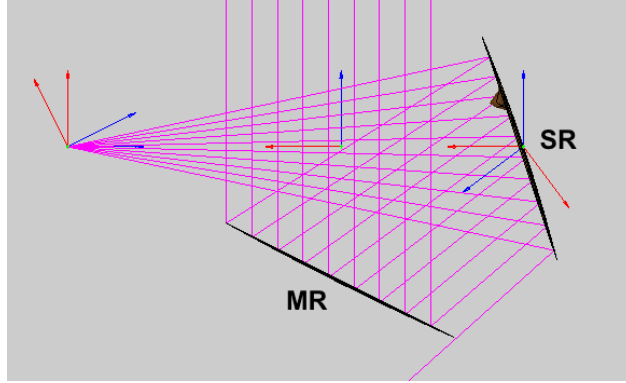


**Figure 4.11:** Location of surface error at the SR (the error is not in scale).

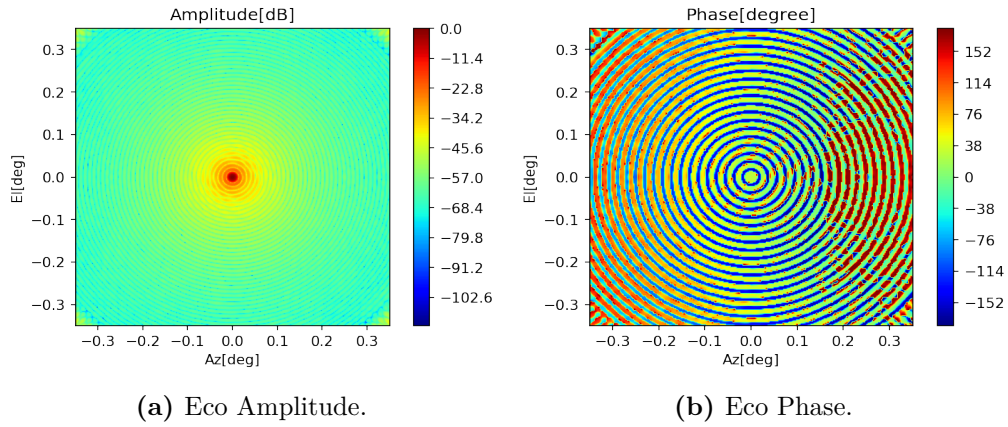


**Figure 4.12:** Far-field diffraction pattern of the CCAT-p when an error is introduced at the SR surface.

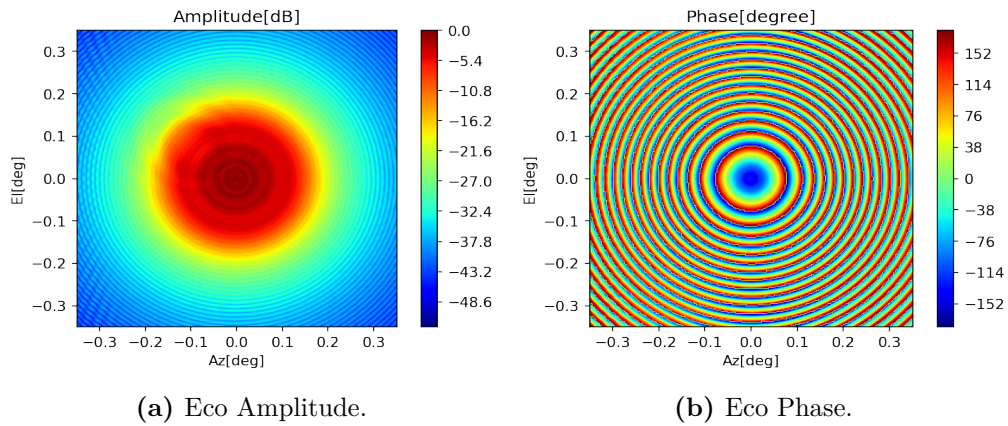


**Figure 4.13:** Near-field diffraction pattern obtained for the CCAT-p telescope with an error at the SR.

# Chapter 5

## Processing and Analysis

In Chapter 4, we presented the holography simulations made with GRASP for the CCAT-p telescope. In these simulations, we obtained data of the diffraction pattern generated by the telescope at the far-field and at the near-field. Three different scenarios were modeled, taking into consideration errors at the reflectors surfaces. Moreover, the feed was located at four different positions of the focal plane.

The holography technique use the Fourier transform relation between the far-field diffraction pattern and the distribution of the electric field at the aperture of the telescope, details in Chapter 2. Through simulations, we now have the data of the patterns at the near and far field. In this chapter we will apply the Fourier transform to this data, to probe how holography will behave for this telescope.

In this chapter we will show the recovered illuminations amplitude and phase for each scenario. Only the more illustrative simulations will be shown. Then, we generate surface error maps and its analysis. Finally we present a correction algorithm and we make an analysis of how the contributions of the errors from each reflector may be separated.

### 5.1 General Strategy

For the processing and analysis of the obtained data we use Python programming language. We developed a library in Python, in which the data obtained by GRASP can be plotted and analyzed. With this library the Fast Fourier Transform algorithm (FFT) is applied to the GRASP simulations data and we recover the electric field distribution (in amplitude and phase) at the aperture of the telescope. This library also incorporates the usual tools for processing and analyzing diffraction patterns data. For more details, the implemented code is in the Appendix of this thesis. We focus our work on the far-field data analysis, as our final objective is the study of the dual surface problem.

When we have recovered the aperture field distribution for each scenario and for each feed

location, we calculate the surface error by using the phase information. We generate surface error maps by subtracting the ideal surface phase distribution to the surfaces with errors phase distribution.

Additionally, we synthesize a fourth scenario using Python. In this scenario the second scenario (error at MR surface) and third scenario (error at SR surface) are combined using the linear properties of the Fourier transform to make a new scenario which simulates the telescope surface with errors at MR and SR. This was done for time issues only, because it can also be done with GRASP.

We simulate a simple correction algorithm over the synthetic scenario that can lower the RMS surface error at each surface. This algorithm is not practical for application, but it serves to illustrate as a first approximation how errors can be disentangled and to demonstrate that the RMS surface error can be diminished.

Finally, we analyze the obtained information and make approximations of how errors behave and how they can be separated into each contribution.

## 5.2 Recovered illuminations and surface error maps

Four illuminations were recovered for each scenario, one for each feed position (a), b), c) and d) as shown in figure 4.1). Only the most significant recovered illuminations will be shown, as in some simulations they are very similar between each other. From this data we can isolate the phase errors caused by the errors at the surfaces. To obtain this, we subtract to each recovered illumination its corresponding ideal-surface illumination. This can be done by using the superposition principle and Fourier transform linearity [35].

### 5.2.1 First scenario: Ideal surfaces

In this scenario, we recover the illuminations corresponding to the telescope with ideal surfaces. Here we will only show the results for the feed on-axis (figure 5.1) and feed off-axis by 50 cm in  $+120^\circ$  from x axis (figure 5.2). The other two positions have very similar illuminations.

#### **Feed on-axis:**

The illumination recovered for the ideal scenario (figure 5.1) is as expected. It has a Gaussian illumination with the nominal edge taper (notice that the feed has a Gaussian distribution with  $-8$  dB edge taper) and a constant phase over the entire aperture.

#### **Feed off-axis position c) :**

If we compare the on-axis case with the off-axis case (figures 5.1 and 5.2 respectively) it can be seen that the center of the Gaussian illumination moves as the feed moved from the

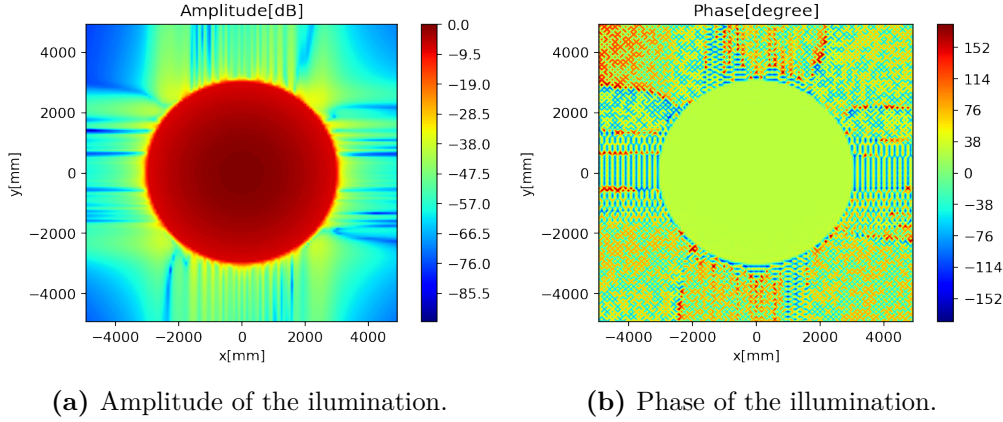


**Figure 5.1:** Amplitude and phase of the CCAT-p telescope obtained at the aperture for an ideal surface.

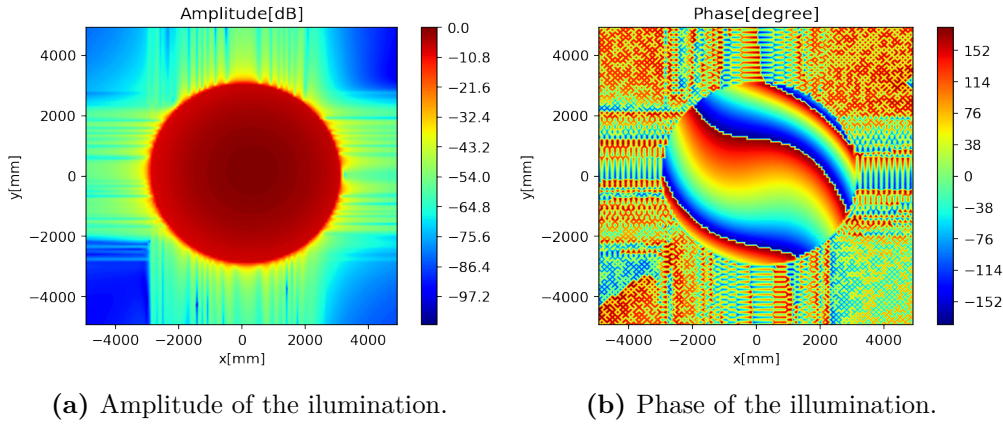


**Figure 5.2:** Amplitude and phase of the CCAT-p telescope obtained at the aperture for an ideal surface. Illumination with an off-axis feed.

center of the focal plane and that the phase is not flat anymore. The pattern that appears at the phase on figure 5.2b is caused by coma aberrations due to moving the feed off-axis. With the corrected surface defined by polynomial equations (see Chapter 3) this is expected to diminish. Anyway, this remnant response has to be taken into consideration to study the contribution from the surfaces. The recovered illuminations for the other positions of the feed are similar, with the center moving to different locations and the phase with a similar pattern but in other orientations.

## 5.2.2 Second scenario: Error at MR surface

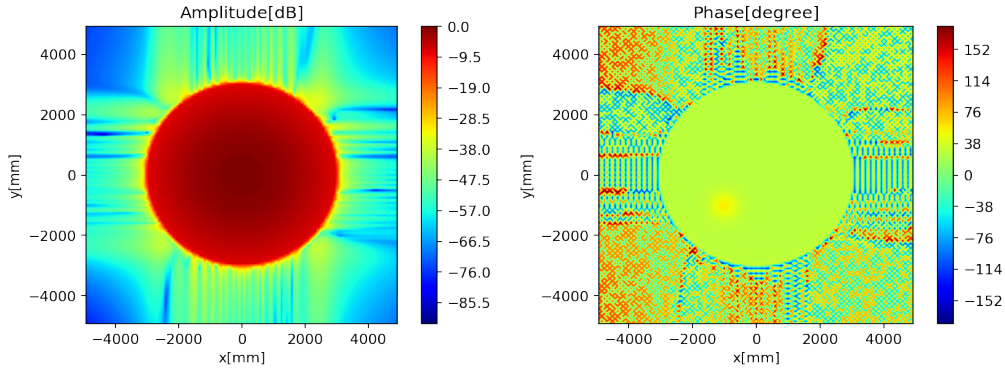
### Recovered Illumination

The second scenario simulates the telescope with surface errors at the MR surface and perfect surface for the SR. The errors at the MR were simulated by a bi-dimensional Gaussian bump of width 60 cm, height of 50  $\mu\text{m}$  and located at  $(x, y) = (-1, -1)$  m. Again, we only show the results for feed on-axis (figure 5.3) and feed off-axis in position c) (figure 5.4) illuminations,



because the results for the other positions are similar.

**Feed on-axis:**



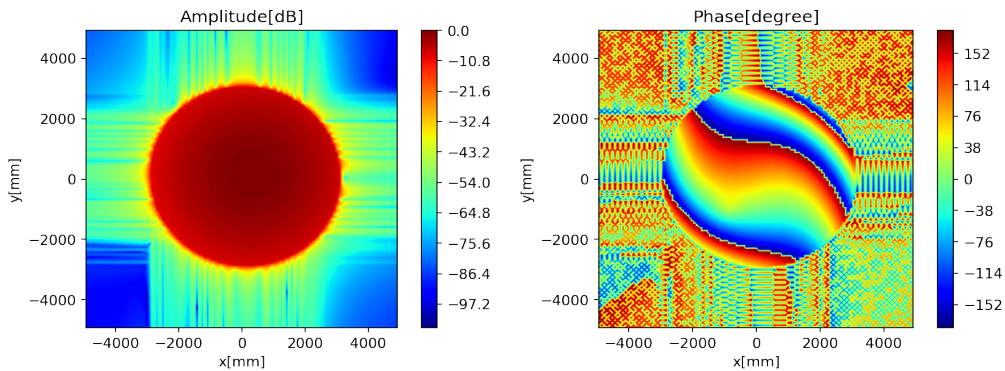
(a) Amplitude of the illumination. (b) Phase of the illumination.

**Figure 5.3:** Amplitude and phase of the CCAT-p telescope obtained at the aperture for a MR simulated with an error.

In figure 5.3 it can be seen that the illumination looks very similar to the perfect surface scenario, but the phase is not plane anymore. It shows a Gaussian perturbation at the location  $(x, y) = (-957, -957)$  mm which is approximately where the bump at M1 was located  $(x, y) = (-1000, -1000)$  mm.

**Feed off-axis position c):**

The illumination presented in figure 5.4 is similar to figure 5.2. However, in the plot of the phase a perturbation in the place of the bump can be distinguished. The illuminations of the other positions of the feed are similar.



(a) Amplitude of the illumination. (b) Phase of the illumination.

**Figure 5.4:** Amplitude and phase of the CCAT-p telescope obtained at the aperture for a MR simulated with an error. Illumination with an off-axis feed.

## Surface error maps:

Because of the superposition principle, the pattern of the second scenario is the resulting pattern of the ideal surface plus the pattern of the surface where the error was introduced. We use this principle to generate surface error maps in Python. To explain this procedure we use the notation

$P$ : diffraction pattern,  
 $I$ : Recovered Illumination,  
 $M$ : Surface error map.

And we use sub-indices for referring to a certain scenario or introduced surface error. For the first scenario (ideal surfaces) we use sub-index 1, and similarly for the other scenarios. For referring to the introduced surface error we use the sub-index E-MR (for a main reflector error) and E-SR (for a sub reflector error). Then the algorithm used for obtaining surface error maps is the following:

$$\begin{aligned} P_2 &= P_{E-MR} + P_1; \\ \text{FFT}(P_2) &= \text{FFT}(P_{E-MR}) + \text{FFT}(P_1); \\ I_2 &= I_{E-MR} + I_1; \\ M_2 &= I_2 - I_1; \\ M_2 &= I_{E-MR}; \end{aligned}$$

In the case of the off-axis feed, it should be noticed that the phase pattern caused by the coma effect is also eliminated since it appears in both the ideal illumination and the second scenario. We show in figure 5.5 the resulting surface map for the on-axis feed. For the other

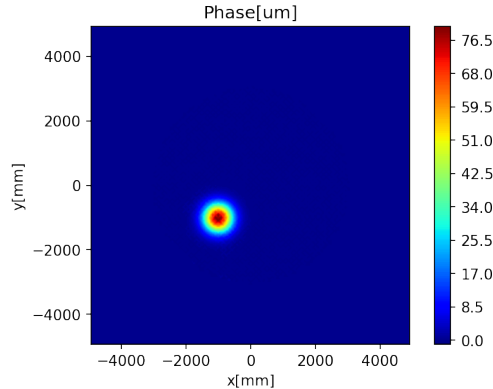


**Figure 5.5:** Surface error map obtained for the second scenario.

three positions the surface map is similar but the location of the error changes. We show in figure 5.6 the maps for the other feed positions.

If we superpose each one of the four surface error maps we obtain the map in figure 5.7 where the four errors appear almost at the same position in the aperture. This means that certain errors may not be distinguishable from one another at the main reflector. The exact



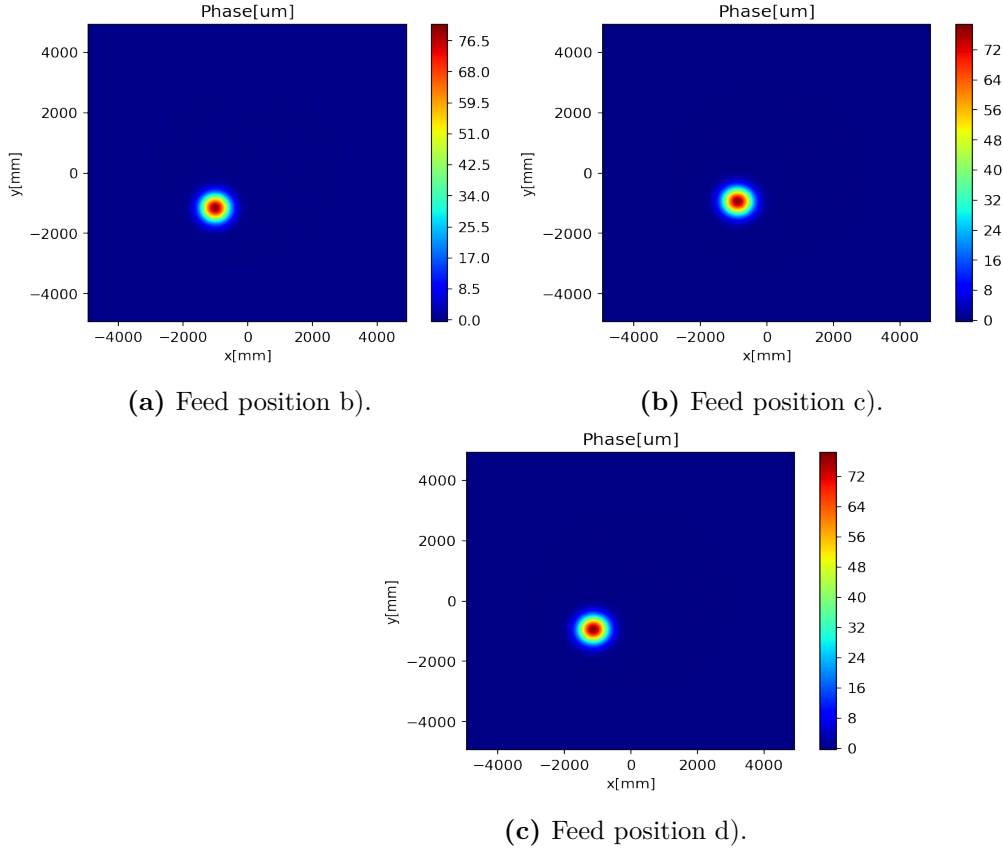


**Figure 5.6:** Surface error maps obtained for the second scenario with the feed off axis in three different positions.

**Table 5.1:** Measured positions of the error at the MR depending on the feed location.

Feed position	X [mm]	Y [mm]	maximum error [um]
on-axis	-1040	-1123	79.910
off-axis b)	-1040	-1206	80.529
off-axis c)	-957	-957	78.510
off-axis d)	-1206	-957	78.210

locations of the errors and their maximum value for each feed position are given in table 5.1.

The difference between where the error appears depending on the receiver position is less than a panel length (600 mm). The maximum errors that were obtained differ from one another because of the angle of incidence ( $\theta_i$ ) of the radiation at their surfaces. The height of the Gaussian bump used as surface error is  $50 \mu\text{m}$ , so the maximum error should be near  $2 \cdot 50 \mu \cdot \cos(\theta_i)$ . However, a difference between this calculation and the obtained results may occur due to diffraction caused by the bump surface. A scheme of this is shown in figure 5.8.

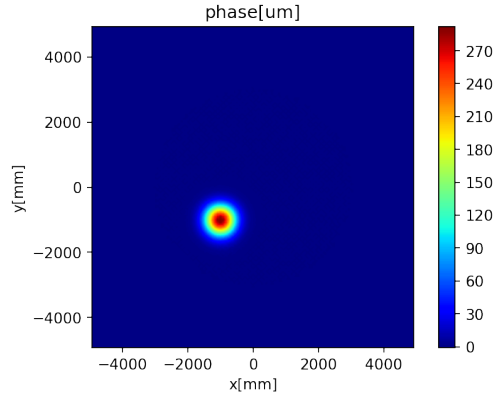


**Figure 5.7:** Addition of the 4 surface error maps for the second scenario (surface error at MR).

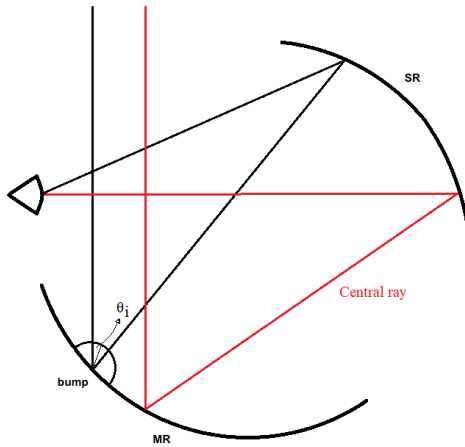


**Figure 5.8:** Scheme of the surface error at MR and how rays reflects from one surface to another.  $\theta_i$  is the angle of incidence at the bump surface .

### 5.2.3 Third scenario: Error at SR surface

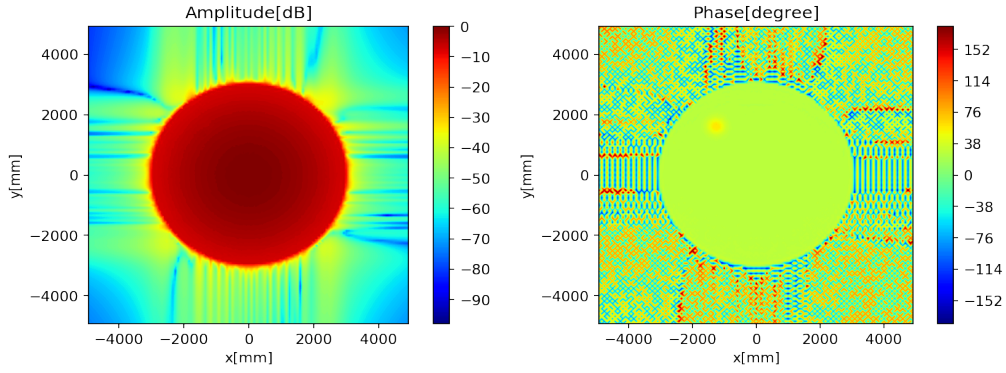
#### Recovered illumination

The third scenario simulates the telescope with surface error at the SR surface and perfect surface for the MR. The error at the SR was simulated by a bi-dimensional Gaussian bump of width 30 cm, height of 50  $\mu\text{m}$  and located at  $(x, y) = (-1, 1)$  m.

Illuminations of feed on-axis and feed off-axis in position c) are shown below. In this scenario, the phase perturbation caused by the error has a considerable change of position from one illumination to another. However, we will show this point in detail in section 5.2 using error maps.

#### Feed on-axis

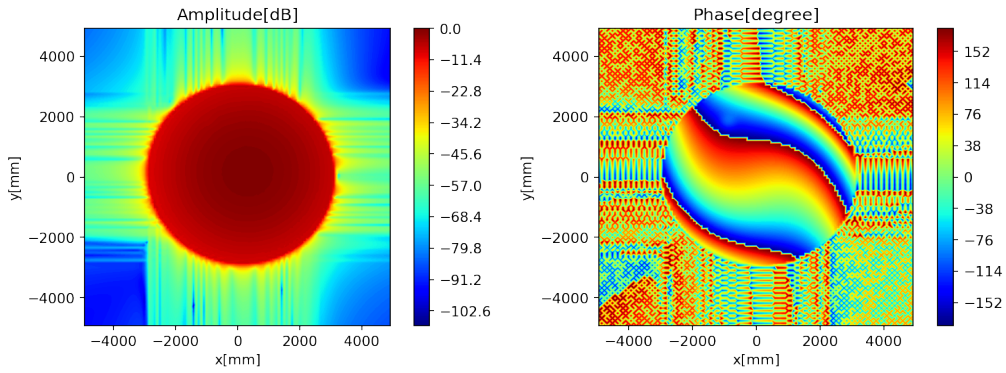
The illumination in figure 5.9a looks similar to figure 5.1a and 5.3a. The phase in figure 5.9b is as expected, flat, with an error bump. This bump appears at the position  $(x, y) = (-957, 1789)$  mm.



(a) Amplitude of the illumination. (b) Phase of the illumination.

**Figure 5.9:** Recovered illumination for the third scenario (error at the SR surface) in amplitude and phase.

Feed off-axis position c):



(a) Amplitude of third scenario with feed off-axis. (b) Phase of third scenario with off-axis feed.

**Figure 5.10:** Recovered illumination for the third scenario with the feed off-axis in three different positions.

The center of the Gaussian illumination moves from the center of the aperture because of the change of position of the feed, similarly than in the other scenarios. The phase information has a pattern caused by coma effect, plus a phase perturbation caused by the error introduced at the SR surface. This is shown in figure 5.10

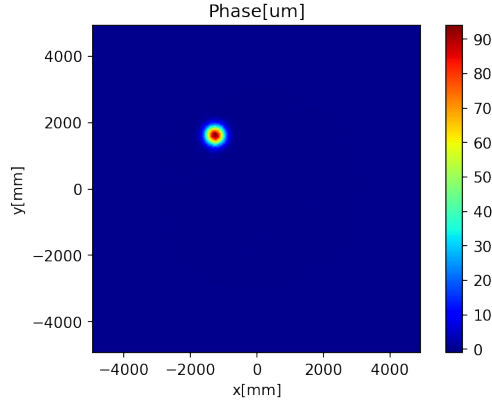


**Figure 5.11:** Surface error map obtained for the third scenario.

**Table 5.2:** Measured positions of the error at the SR depending on the feed location.

Feed position	X [mm]	Y [mm]	maximum error [um]
on-axis	-1290	1623	93.622
off-axis b)	-1290	1112	95.024
off-axis c)	-957	1789	92.580
off-axis d)	-1623	1789	94.224

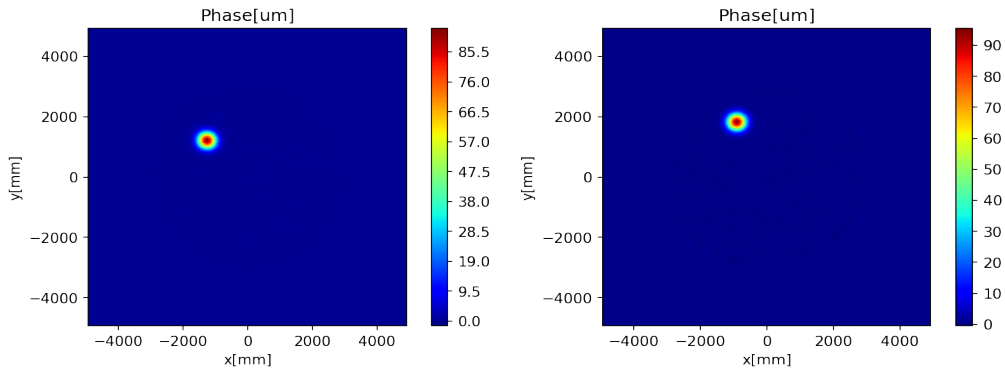
### Surface error maps:

We generate surface error maps with the same algorithm used in the second scenario as follows:

$$\begin{aligned}
 P\_3 &= P\_E\text{-SR} + P\_1; \\
 \text{FFT}(P\_3) &= \text{FFT}(P\_E\text{-SR}) + \text{FFT}(P\_1); \\
 I\_3 &= I\_E\text{-SR} + I\_1; \\
 M\_3 &= I\_3 - I\_1; \\
 M\_3 &= I\_E\text{-SR};
 \end{aligned}$$

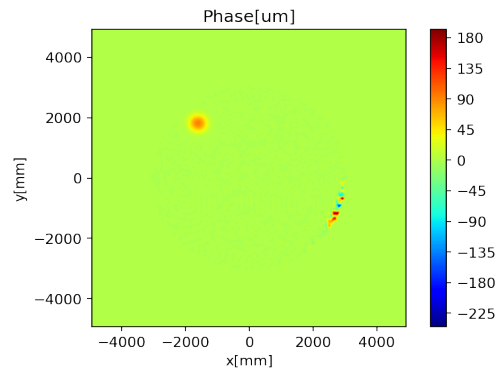
Again, for the off-axis feed the phase pattern caused by coma effect is eliminated, as it appears in the ideal illumination and the third scenario illumination. We show in figure 5.11 the resulting surface map for the on-axis feed. In figure 5.12 the surface error maps for the other three positions are shown. We superpose each one of the four surface error maps to obtain the map in figure 5.13. In this figure it can be easily noticed that errors at the SR change their position at the aperture depending on the feed location. A numeric error appears at the right side of the aperture. This error only appears in one of the maps (position d) and might be caused by diffraction at the edge of the SR.

The exact locations of the errors and their maximum value for each feed position are given in table 5.2. The position of the error for each feed location changes considerably. This happens because the angle of incidence ( $\theta_i$ ) of the ray from the feed to the SR changes significantly between each feed position. As in the second scenario, the error amplitude should be near



(a) Feed position b).

(b) Feed position c).



(c) Feed position d).

**Figure 5.12:** Surface error maps for the third scenario. Shown for the three positions of the feed.

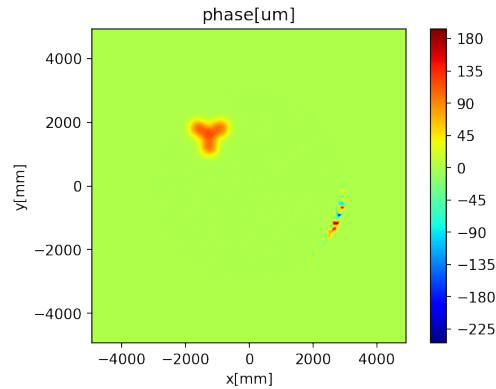


**Figure 5.13:** Addition of the 4 surface error maps for the third scenario (surface error at SR).

$2 \cdot 50 \mu \cdot \cos(\theta_i)$  and the difference between the calculated and the obtained amplitude may be due to diffraction. In figure 4.11 a scheme of this is shown.

It is noticed that the changes are proportional to the change in the position of the feed, forming an image comparable to figure 4.1.

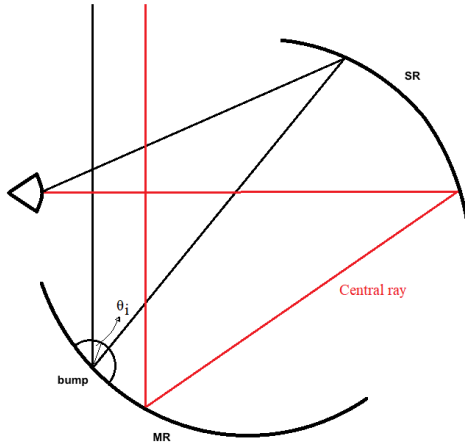


**Figure 5.14:** Scheme of the surface error at SR and how rays reflect from one surface to another.  $\theta_i$  is the angle of incidence at the bump surface .

## 5.2.4 Fourth scenario: Synthetic scenario with errors at MR and SR surfaces

We have synthesized a fourth scenario in which there is an error at the MR surface and at the SR surface. For this purpose we have used the data obtained for the other three scenarios. We want to obtain a Gaussian bump of width 60 cm, height of 50  $\mu\text{m}$ , located at  $(x, y) = (-1, -1)$  m in the MR and a Gaussian bump of width 30 cm, height of 50  $\mu\text{m}$ , located at  $(x, y) = (-1, 1)$  m in the SR. This is made by using the linear properties of the Fourier transform and the superposition principles for the electric field [35].

The surfaces with errors were simulated by adding to the perfect surfaces an error (two-dimensional Gaussian function). The radiation patterns of the surfaces with errors are the superposition of the ideal surface pattern with the error pattern. To make the synthetic scenario, we have added to the ideal pattern, the patterns of the error in the MR and the pattern of the error in the SR. Below we show the algorithm, implemented in Python, that was used for this.

$$\begin{aligned}
 P_{\text{E-MR}} &= P_2 - P_1; \\
 P_{\text{E-SR}} &= P_3 - P_1; \\
 P_4 &= P_{\text{E-MR}} + P_{\text{E-SR}} + I_1; \\
 P_4 &= P_2 + P_3 - P_1;
 \end{aligned}$$

Using this algorithm we obtain the synthetic pattern shown in figure 5.15. This procedure has been done for the four positions of the feed, but here we only show the on-axis pattern. We can see that the pattern in figure 5.15a is a combination of patterns in figures 4.9a and 4.12a.

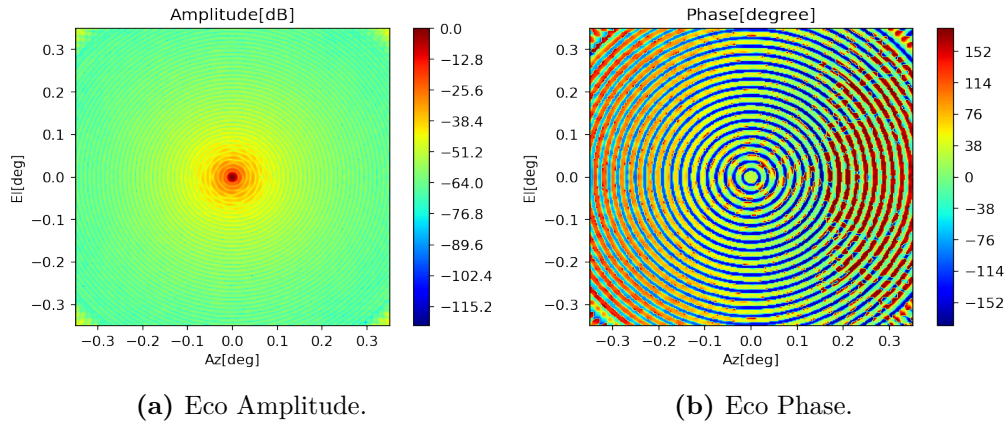


**Figure 5.15:** Far-field diffraction pattern obtained for the fourth scenario in amplitude and phase.

## Recovered illumination

The next step is to apply the Fourier transform to the synthetic pattern, to recover the illumination of this fourth scenario. This procedure has been applied to the four positions of the feed, but we only show the illuminations for the central feed in figure 5.16 and for the feed off-axis at position c) in figure 5.17.

## Feed on-axis

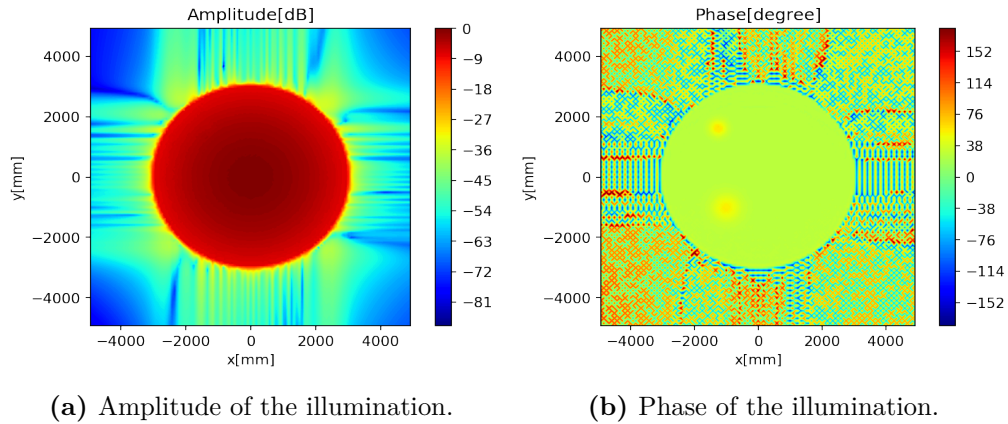
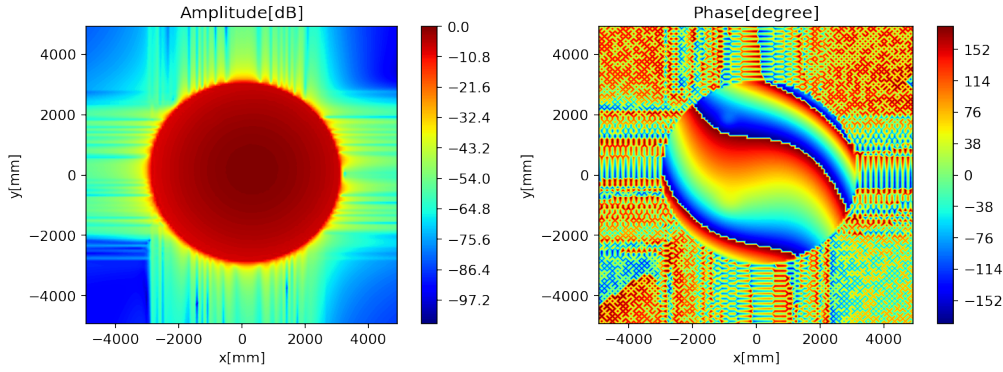


**Figure 5.16:** Electric diffraction pattern obtained for the fourth scenario in amplitude and phase.



Feed off-axis position c):



(a) Amplitude of the illumination.

(b) Phase of the illumination.

**Figure 5.17:** Illumination obtained for the phase scenario for the three positions of the feed.

In figure 5.16 and figure 5.17 It can be seen in figures 5.16 and 5.17 that amplitudes are very similar to the other scenarios. Moreover, now it appears a phase perturbation in the position of the error at MR and another at the position of the error at SR. This effect happens for all the four positions of the feed.

### Surface error maps

By applying the FFT python algorithm to the synthetic pattern and subtracting the ideal illumination we obtain its surface error map:

$$\begin{aligned}
 P_4 &= P_2 + P_3 - I_1; \\
 \text{FFT}(P_4) &= \text{FFT}(P_2) + \text{FFT}(P_3) - \text{FFT}(P_1); \\
 I_4 &= I_2 + I_3 - I_1; \\
 I_4 &= I_{E-MR} + I_{E-SR} + I_1; \\
 M_4 &= I_4 - I_1; \\
 M_4 &= I_{E-MR} + I_{E-SR};
 \end{aligned}$$

This procedure has been applied to the four positions of the feed for each scenario. We show in figure 5.18 the surface error map for the on-axis feed. The resulting surface-error map is the addition of the error maps of the second scenario and third scenario. We have added the four surface error maps (one for each feed position) resulting in the map shown in figure 5.19. The positions of the errors are the same as in the second and third scenario. They are summarized in table 5.3.

We can see, from figure 5.19 and table 5.3, that the positions of the errors at the MR move some cm for each position of the feed. However, this distance taking in consideration that the panels measure approximately 60 cm, these distances are negligible. On the other hand, errors at the SR move considerably more with the change of position of the feed. This changes in the positions of the errors are due to parallax, and can be calculated by geometrical optics (not taking into account diffraction effects). Distances are proportional to the change in the



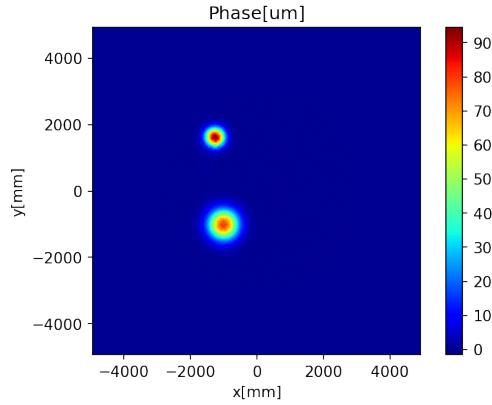


**Figure 5.18:** Surface error map obtained for the fourth scenario.

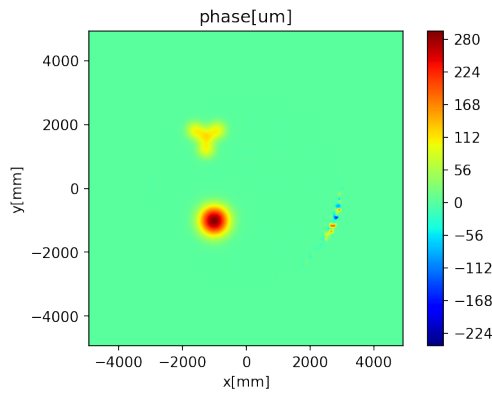


**Figure 5.19:** Addition of the 4 surface error maps for the synthetic scenario.

feed position, as the location of the error at the aperture depends on the angle of incidence of the ray in the error surface.

### 5.3 Compensating the RMS surface error

The main reason for doing holography in the CCAT-p telescope is for correcting the reflector surfaces. This problem is measured as the surface error RMS, and a goal of 7–10  $\mu\text{m}$  has been set. Since each reflector surface must be corrected, it is necessary to separate the holography measurements into contribution of each reflector at the aperture.

Finding the surface error of each reflector needs a more exhaustive analysis, but, given the previous work, it seems to be possible. Here we show an algorithm to diminish the surface error RMS without separating the errors in the MR and SR.

The algorithm starts with holography measurements of the aperture at the four feed positions. Then, it generates four surface error maps obtained by following the procedure shown in section 5.1 to correct each one of the surfaces, i.e MR surface and SR surface. After the cor-

**Table 5.3:** Measured positions of the errors at the MR and SR depending on the feed location for the fourth scenario.

Feed position	X [mm]	Y [mm]	maximum error [um]
MR surface error			
on-axis	-1040	-1123	79.910
off-axis b)	-1040	-1206	80.529
off-axis c)	-957	-957	78.510
off-axis d)	-1206	-957	78.210
SR surface error			
on-axis	-1290	1623	93.622
off-axis b)	-1290	1112	95.024
off-axis c)	-957	1789	92.580
off-axis d)	-1623	1789	94.224

rection, a new holography measurement of the telescope is taken. With this new measurement we calculate the new error at the aperture and correct each reflector surface again. In each iteration the RMS surface error is recorded. Below and in figure 5.20 we present this algorithm.

1) We acquire the telescope diffraction patterns for each feed position:  
(Pattern 1, Pattern 2, Pattern 3, Pattern 4)

2) We recover the correspondent illuminations by applying the FFT algorithm to each pattern:  
(Illumination 1, Illumination 2, Illumination 3, Illumination 4).

3) We make error maps by subtracting the measured patterns with the ideal patterns (known by simulations):  
(error map 1, error map 2, error map 3, error map 4)

4) We create two mean error maps. The first is made by adding each error map and dividing it by 4 (E1\_0). The second by adding each error map shifted by a determined length (that will be explained later) and divided by 4 (E2\_0).

$$E1\_0 = (\text{error map 1} + \text{error map 2} + \text{error map 3} + \text{error map 4})/4$$

$$E2\_0 = (\text{shift}(\text{error map 1}) + \text{shift}(\text{error map 2}) + \text{shift}(\text{error map 3}) + \text{shift}(\text{error map 4}))/4$$

5) We correct each reflector surface by subtracting the error maps obtained at step 4). We call SurfaceMR the main reflector surface and surfaceSR the sub reflector surface:

$$\text{SurfaceMR\_1} = \text{SurfaceMR} - E1\_0$$

$$\text{SurfaceSR\_2} = \text{SurfaceSR} - E2\_0$$

6) We return to step 1) and iterate. The surface error RMS of the reflectors is recorded after each iteration.

Step 1) uses holography to measure the four diffraction patterns for each measurement position. Step 2) uses Python, as in section 5.2, to apply the FFT to each pattern and recover the corresponding illuminations. Then, in step 3) the error maps are obtained by subtracting to each measured pattern its ideal pattern which was calculated previously by simulations.

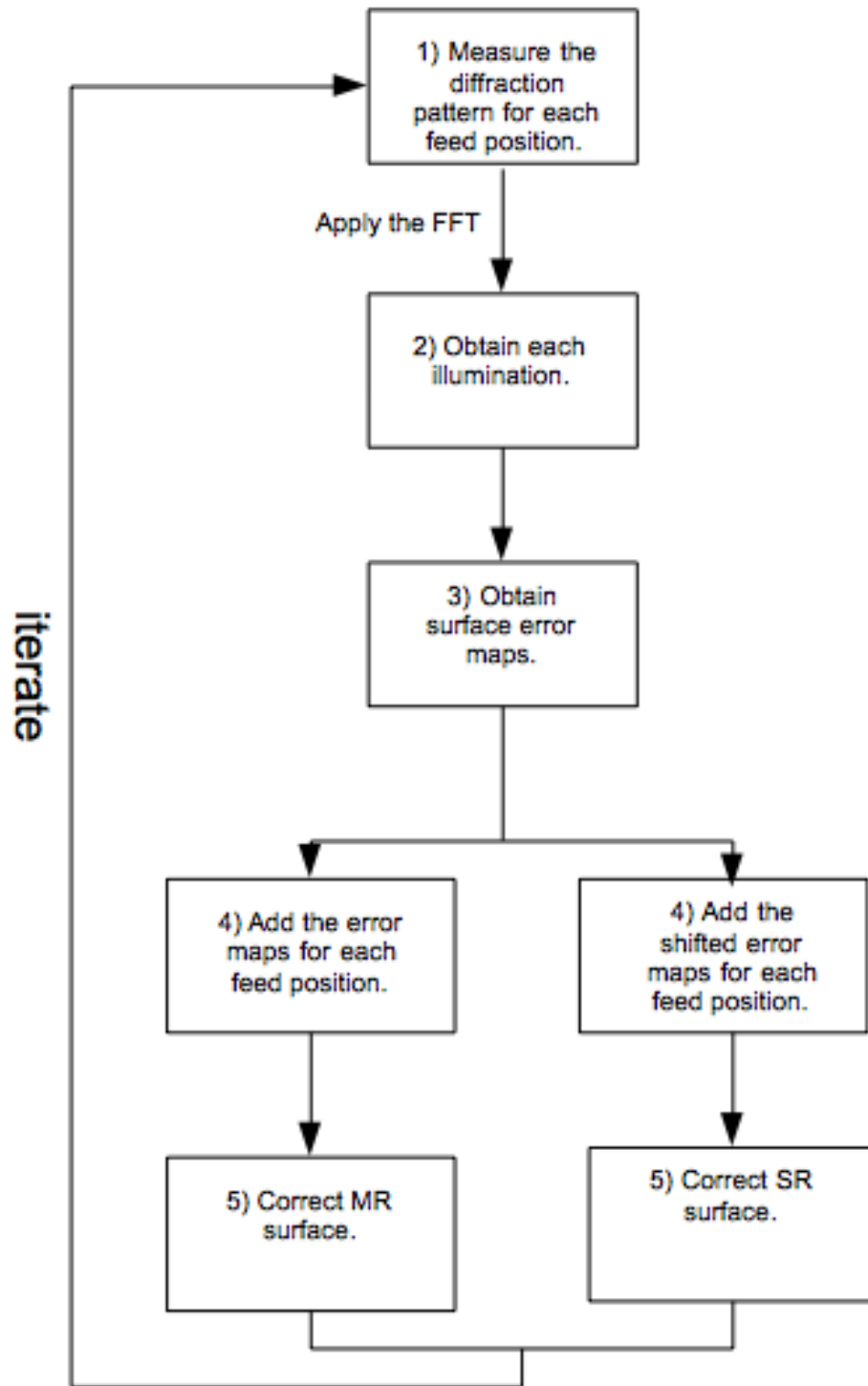
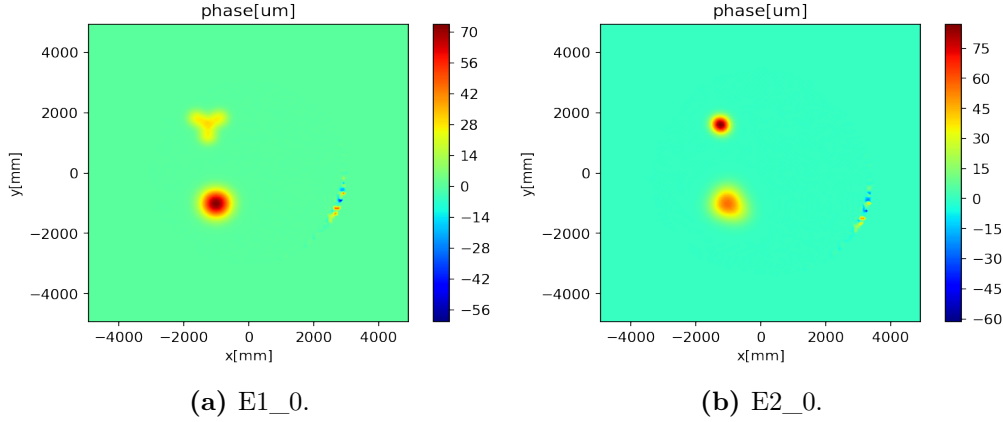


Figure 5.20: Surface error diminution algorithm.



**Figure 5.21:** Error maps obtained for each surface by calculating the mean between their correspondents surface error maps.

Step 4) uses the four obtained error maps to make two mean error maps. First, by adding the four error maps and dividing the result by 4, we obtain a map in which the errors at the main reflector appear almost at the same position regardless of the receiver position. Then, we shift each error map by a length that makes the sub reflector errors coincide in their position. The shift length in each case was calculated as the change of position of the SR error shown in table 5.3. This will cause that when we correct each reflector in step 5), the error belonging to each reflector will be almost eliminated. We introduce an additional error to each reflector corresponding to the other reflector’s error, but its magnitude will be divided by 4. In figure 5.21 we show how the mean error maps ,E1\_0 and E2\_0, look for the fourth scenario.

The correction will diminish the surface error because the corrected error will overcome the introduced error. The RMS surface error is calculated for each surface and then we return to step 1) , in which new holography measurements are made to the corrected surfaces.

In this work we simulated this procedure by using the GRASP holography simulations and Python. Below we show the results obtained by applying the correction algorithm to the fourth scenario (errors at MR and SR surfaces). First we show in figure 5.22 the error maps of each surface before applying the correction algorithm. The original error maps correspond to the surface error maps shown in section 5.2, as we used the simulations with errors at the MR and at the SR. In figure 5.23 we show how the RMS surface error of each reflector diminishes as the number of iterations increases, we applied the algorithm 30 times. The error diminishes in both surfaces with the correction algorithm as the number of iterations increases. However, the maximum error is still considerable. Then in figure 5.24 we show how the surface error map for each reflector looks after 30 iterations. It is seen that the algorithm spreads the errors over the surfaces, resulting in an overall diminution of the surface error. The structure at the right of the maps comes from the spreading of the numerical error present in position d) simulation at the third scenario. In this work the surface errors simulated by GRASP are low and well defined, so the RMS surface errors in this case start satisfying the  $<7\mu$  m RMS error. To test this algorithm with a more realistic case, the surfaces of the reflectors should be simulated with a more realistic error distribution. For example, random errors distributed all over the surfaces could be modeled in which case the

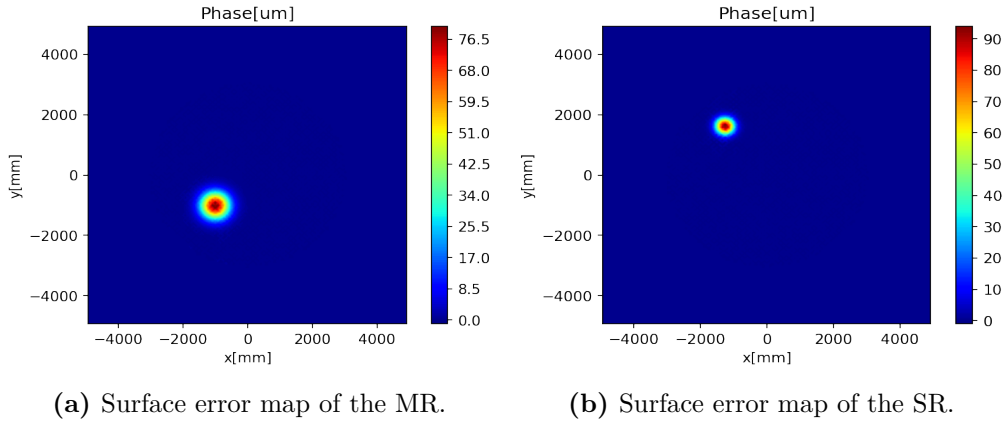


**Figure 5.22:** Surface error maps before applying the correction algorithm.

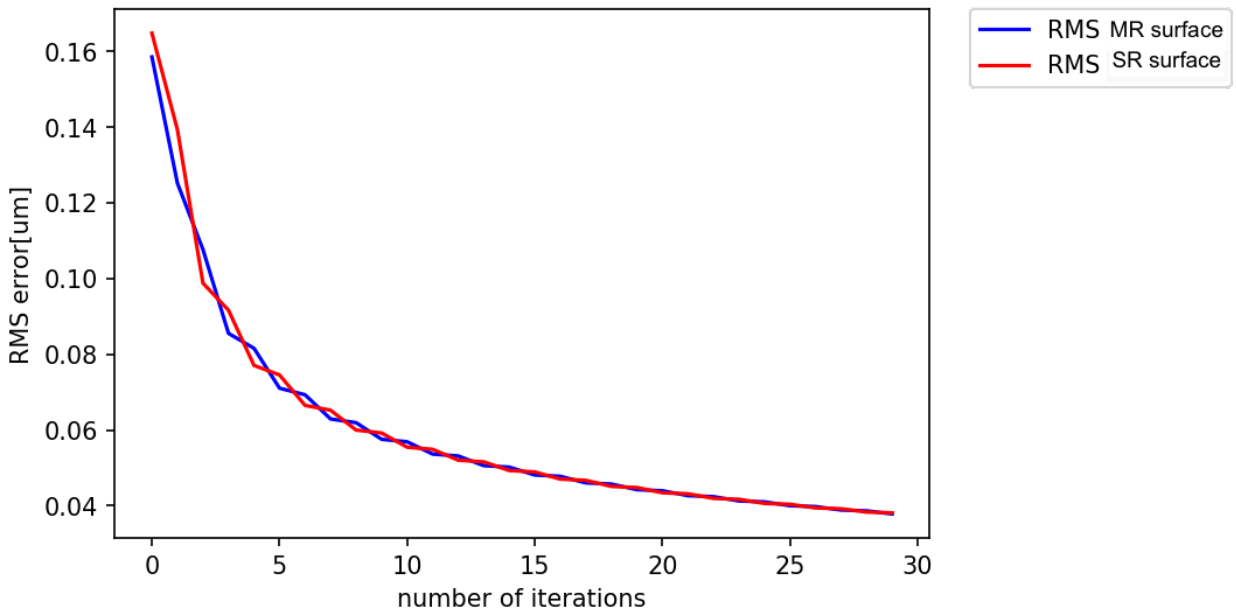


**Figure 5.23:** RMS surface error diminution by applying the algorithm for 30 iterations.

diminution of RMS errors should be slower and might not converge. Another issue is that the shift length was easy to calculate in this simulations because of the well defined errors, but with a more realistic distribution this might not be possible. This method requires to make an holography measurement, correct and measure again. To apply this on-site would be very impractical as, with a more realistic error distribution, many iteration could be needed. For this reasons, it would be more practical finding a method to identify where the errors come from.

## 5.4 Separation of errors

For an adequate correction of the telescope surface we need to be able to separate the holography measurement into the contributions of each reflector surface. To solve this problem

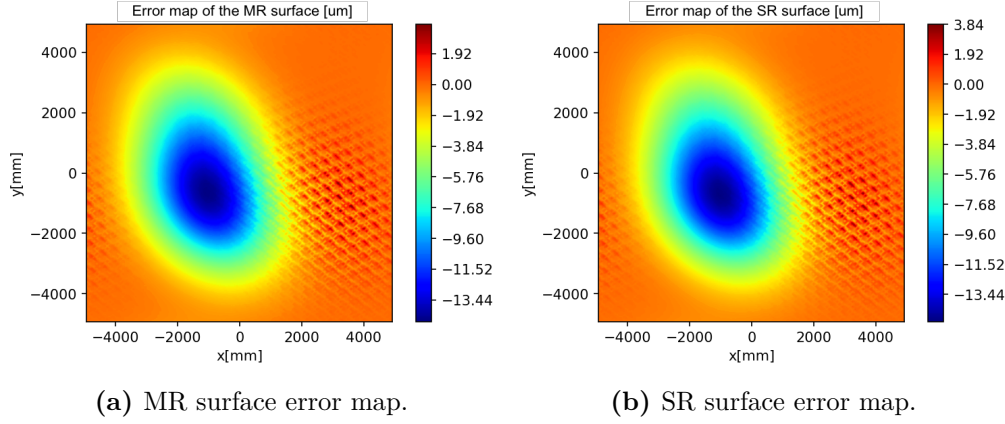


**Figure 5.24:** Surface error maps of each reflector after 30 iterations.

more simulations and analysis are required. With the approach of taking measurements into four different positions of the focal plane, it should be possible. Here we make an analysis of how this could be done using the four error maps provided by the holography system.

We have seen in section 5.1 that the change of position of errors at the main reflector is almost negligible compared with the change of position of errors at the secondary reflector. If we take into account that the telescope surface should begin with a low surface error RMS (the construction company should provide this feature), the change of position in the aperture plane of errors can be estimated by geometrical optics. This is because with small errors we can calculate the position of the error only by its position at the reflector surface and feed location, underestimating the change caused by the shape error. With this information, we could calculate for each position of the feed where a SR error in a determinate position should arrive at the aperture plane.

If we have the four surface error maps [lets call them  $Map1(x, y)$ ,  $Map2(x, y)$ ,  $Map3(x, y)$  and  $Map4(x, y)$ ], and find functions which determine the aperture position and amplitude of an SR error depending on the feed location [ $f1(x, y)$ ,  $f2(x, y)$ ,  $f3(x, y)$ ,  $f4(x, y)$ ], we could separate the surface errors at each reflector (MR\_error and SR\_error) using the following equation system,

$$\begin{aligned}
 Map1(x, y) &= MR\_error(x, y) + f1(SR\_error(x, y)) \\
 Map2(x, y) &= MR\_error(x, y) + f2(SR\_error(x, y)) \\
 Map3(x, y) &= MR\_error(x, y) + f3(SR\_error(x, y)) \\
 Map4(x, y) &= MR\_error(x, y) + f4(SR\_error(x, y)).
 \end{aligned}$$

This system of equations neglects the change in MR errors, taking them as constant.

The functions  $f1$ ,  $f2$ ,  $f3$  and  $f4$ , according to what has been observed in simulations, are mainly a shift in the position of the error and a multiplying factor given by the angle of incidence ( $\cos(\theta_i)$ ). The proposed functions would look like :

$$f(SR\_error(x, y)) = \cos(\theta_i) * (SR\_error(x + H_x(x, y), y + H_y(x, y))) \quad (5.1)$$

The  $H_x(x, y)$  and  $H_y(x, y)$  functions are the shifts in the position of errors, this distance could

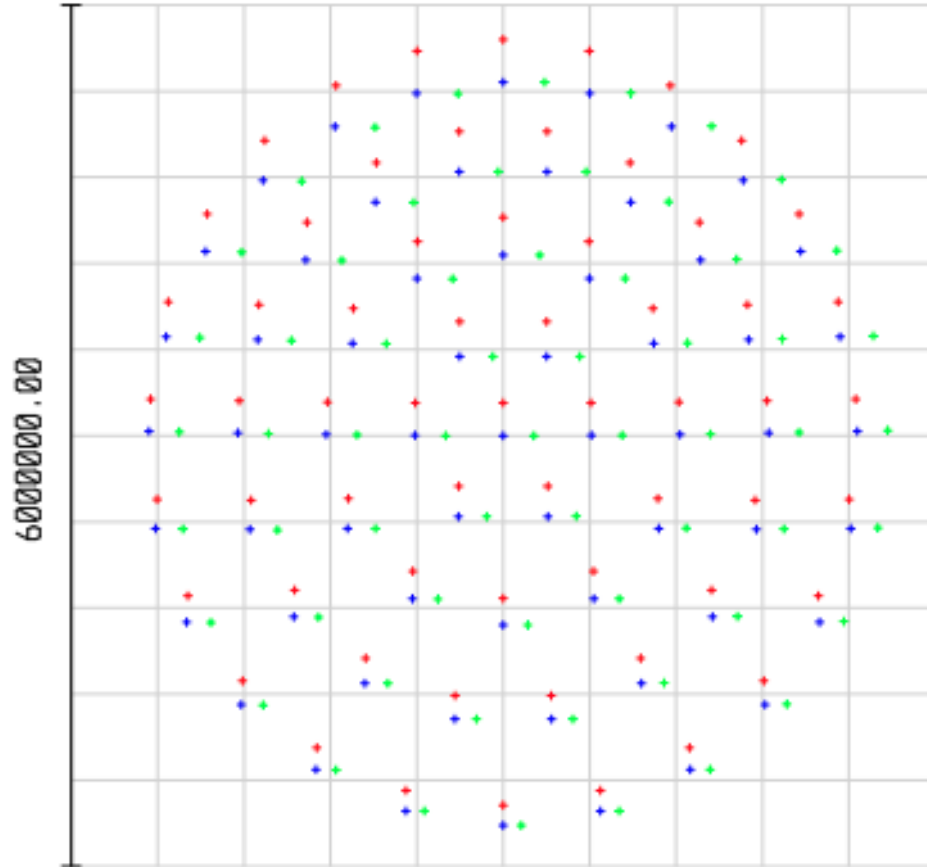


**Figure 5.25:** Rays at the aperture plane depending on the originating position in the focal plane [29].

be found by geometrical optics for each feed position.  $H_x(x, y)$  and  $H_y(x, y)$  functions depend on  $(x, y)$  because the reflectors are more separated in the upper portion of the telescope than at the lower portion. This is illustrated by figure 5.25 given by [29]. It is a diagram obtained by Zemax software that shows how rays arrive in the aperture of the telescope depending on the originating position on the focal plane. In the figure blue, red and green rays correspond to positions in the focal plane of  $(0,0)$ ,  $(2,0)$  and  $(0,2)$  degrees respectively. If we take the approximation of errors at the MR being at the same position and have calculated the functions  $H_x(x, y)$  and  $H_y(x, y)$ , we could find the SR map by making a fit that complies with this system of equations.

## 5.5 Conclusions

In this chapter we show the results obtained by analyzing and processing the diffraction patterns of the CCAT-p telescope obtained by GRASP simulations. We were able to recover the illumination of the aperture, by applying the FFT, and probe how holography would work for this telescope. Using the measurements with the feed at four different positions, we showed that errors at the MR and at the SR change their position at the aperture. Errors

at the SR change significantly their position at the aperture depending on the feed location. We created a correction algorithm that shows how the surfaces could be corrected without separating the contributions of each one of them. However, this algorithm is impractical for implementation so the separation of errors should be studied in more details. Finally, we studied the feasibility of separating errors presenting a system of equations that modelates how errors behave.



# Chapter 6

## Conclusions and future work

### 6.1 Conclusions

For achieving the desired accuracy of  $10^{-7}$   $\mu\text{m}$  RMS in the CCAT-p telescope, it is fundamental to use a technique for measuring the surfaces errors. The selected technology is millimeter-wave holography, because its proven results and relative easiness of implementation.

For implementing an accurate holography system, previous design and simulations are crucial. In this work we have successfully made near-field and far-field simulations applying the given design parameters. Near-field simulations were required because of the source location and far-field simulations for the overall system performance. The far-field simulations, as expected, showed the circular symmetry and low cross polarization characteristics of the Crossed-Dragone telescope.

The concept of measuring in four positions of the focal plane was applied in the simulations by changing the location of the focal plane. We obtained a change of position of the maximum amplitude according to the scale factor.

Errors at the reflectors surfaces were successfully modeled and we noticed the change in the patterns caused by them. The surface errors introduced in the simulations appeared in the phase data as expected by using the FFT algorithm.

Subtracting the illuminations obtained under different scenarios and the ideal illumination, surface error maps were made. The surface error maps obtained were concordant to the simulations.

Using the four measuring positions of the feed we identified a different behaviour between errors at the main reflector and errors at the secondary reflector. Errors at the SR experiment a substantial change in their position at the aperture depending on the feed location. Errors at the MR experiment a small change in their position depending on the feed location. However, this should be proven with other types of errors. The small change in the positions

of errors at the MR suggests that there may be errors that can be distinguished from one another. By measuring the change in the position of the error at the secondary, it is noticed that it is proportional to the change of position of the feed. This displacement could be estimated by geometrical optics disregarding the error shape.

A simple algorithm was used for correcting each surface and it effectively reduced the surface error RMS of both reflectors. However, this was performed using simulated scenarios that have very low and punctual errors. This algorithm should be proven with a more realistic error such as a randomly distributed error all over the surfaces. Moreover, this algorithm would be impractical to implement, as it would be needed to correct and measure many times before achieving a good accuracy.

The behaviour of the errors was studied and a way of separating them was proposed. This assumption neglects the changes in errors at the MR and approximates changes in errors at the SR as a shift in their position and a multiplying factor (depending on the angle of incidence). With this, a fit algorithm could be made to find errors at the SR.

This work was a probe of concept of the proposed holography implementation. We have accomplished a closer view to the problem and how to carry on with the future work. The issue of separating errors measured by the holography system into each reflector contribution is complex and need more simulations and analysis. However, using a basic model we probe to be possible.

## 6.2 Future work

The separation of errors into each reflectors contribution has to be addressed in future work. To achieve this, more realistic errors should be simulated, like random errors distributed all over the reflectors. Panel distribution should also be taken into account, as it would be easier to identify were errors are coming from.

The movement of errors coming from the SR surface and measured at the aperture plane should be studied in more detail. If the change between error maps of each feed position can be approximated by a mathematical function, this could be the way of separating the reflectors contribution.

Image processing and stereoscopic vision algorithms could be used with the four error maps to identify and distinguish errors coming from the MR and the SR.

# Chapter 7

## Bibliography

- [1] N. Button, "Submillimeter Astronomy", Hosting.astro.cornell.edu. [Online]. Available: <http://hosting.astro.cornell.edu/~spifiweb/Motivation.html>. [Accessed: 09-Dec- 2018].
- [2] "CCAT : History", Ccatobservatory.org. [Online]. Available: <http://www.ccatobservatory.org/index.cfm/page/about-ccat/History.htm>. [Accessed: 09-Dec- 2018].
- [3] "Astroclimatology of Chajnantor (Chile)", Eso.org. [Online]. Available: <http://www.eso.org/gen-fac/pubs/astclim/espas/radioseeing/>. [Accessed: 09-Dec- 2018].
- [4] "The Best Site for the Biggest Telescope: The VLT Goes to Paranal", www.eso.org, 2018. [Online]. Available: <https://www.eso.org/public/news/eso9015/#2>. [Accessed: 15-Dec- 2018].
- [5] "Astronomy Program | Astronomía", Conicyt.cl. [Online]. Available: <https://www.conicyt.cl/astronomia/astronomy-program/>. [Accessed: 09-Dec- 2018].
- [6] M. Niemack, "Designs for a large-aperture telescope to map the CMB 10× faster", Applied Optics, vol. 55, no. 7, p. 1686, 2016.
- [7] "CCAT : Telescope Details", Ccatobservatory.org, 2018. [Online]. Available: [http://www.ccatobservatory.org/index.cfm/page/observatory/telescope\\_details.htm](http://www.ccatobservatory.org/index.cfm/page/observatory/telescope_details.htm). [Accessed: 15-Dec- 2018].
- [8] D. Rochblatt, "Holographic measurements of the NASA-JPL Deep Space Network antennas", 1998 IEEE Aerospace Conference Proceedings (Cat. No.98TH8339).
- [9] C. Dragone, "Offset Multireflector Antennas with Perfect Pattern Symmetry and Polarization Discrimination", Bell System Technical Journal, vol. 57, no. 7, pp. 2663-2684, 1978.
- [10] "CCAT : Science", Ccatobservatory.org. [Online]. Available: <http://www.ccatobservatory.org/science/>.

[ccatobservatory.org/index.cfm/page/science.htm](http://ccatobservatory.org/index.cfm/page/science.htm). [Accessed: 09- Dec- 2018].

- [11] H. Kiuchi, M. Yamada, M. Sugimoto, H. Saito, T. Matsui and M. Saito, "A Holography Receiver Design for the ALMA Submillimeter Antenna Surface Measurement", *IEEE Transactions on Instrumentation and Measurement*, vol. 62, no. 10, pp. 2763-2772, 2013.
- [12] D. Morris et al., "Surface adjustment of the IRAM 30m radio telescope", *IET Microwaves, Antennas Propagation*, vol. 3, no. 1, p. 99, 2009.
- [13] R. Güsten, L. Nyman, P. Schilke, K. Menten, C. Cesarsky and R. Booth, "The Atacama Pathfinder EXperiment (APEX) – a new submillimeter facility for southern skies –", *Astronomy Astrophysics*, vol. 454, no. 2, pp. L13-L16, 2006.
- [14] J. Baars, R. Lucas, J. Mangum and J. Lopez-Perez, "Near-Field Radio Holography of Large Reflector Antennas", *IEEE Antennas and Propagation Magazine*, vol. 49, no. 5, pp. 24-41, 2007.
- [15] 2018. [Online]. Available: <https://www.astro.uni-koeln.de/nanten2/node/25>. [Accessed: 16- Dec- 2018].
- [16] Itu.int, 2018. [Online]. Available: [https://www.itu.int/dms\\_pub/itu-r/opb/rep/R-REP-RS.2194-2010-PDF-E.pdf](https://www.itu.int/dms_pub/itu-r/opb/rep/R-REP-RS.2194-2010-PDF-E.pdf). [Accessed: 16- Dec- 2018].
- [17] R. Hills, N. Reyes and U. Graf, "Plan for Holography measurements of CCAT-prime using an Artificial Source", 2018.
- [18] C. Granet, "Designing classical Dragonian offset dual-reflector antennas from combinations of prescribed geometric parameters", *IEEE Antennas and Propagation Magazine*, vol. 43, no. 6, pp. 100-107, 2001.
- [19] "Specifying Wavefront vs. Surface Error in Aspheres", *Aperture Optical Sciences - Optical Components*, 2018. [Online]. Available: <http://www.apertureos.com/off-axis/specifying-wavefront-vs-surface-error-aspheres/>. [Accessed: 16- Dec- 2018].
- [20] J. Ruze, "Antenna tolerance theory-A review", *Proceedings of the IEEE*, vol. 54, no. 4, pp. 633-640, 1966.
- [21] von Hoerner, "Design of large steerable antennas", *The Astronomical Journal*, vol. 72, p. 35, 1967.
- [22] J. Baars, R. Martin, J. Mangum, J. McMullin and W. Peters, "The Heinrich Hertz Telescope and the Submillimeter Telescope Observatory", *Publications of the Astronomical Society of the Pacific*, vol. 111, no. 759, pp. 627-646, 1999.
- [23] D. Rochblatt and B. Seidel, "Microwave antenna holography", *IEEE Transactions on Microwave Theory and Techniques*, vol. 40, no. 6, pp. 1294-1300, 1992.
- [24] Gb.nrao.edu, 2018. [Online]. Available: <http://www.gb.nrao.edu/MetConf/talks/Wednesday/Kesteven.pdf>. [Accessed: 16- Dec- 2018].

- [25] J. Delannoy, "The design of high frequency antennas", International Astronomical Union Colloquium, vol. 131, pp. 15-25, 1991.
- [26] T. Essinger-Hileman, J. Appel, J. Beal, H. Cho, J. Fowler, M. Halpern, M. Hasselfield, K. Irwin, T. Marriage, M. Niemack, L. Page, L. Parker, S. Pufu, S. Staggs, O. Stryzak, C. Visnjic, K. Yoon, Y. Zhao, B. Young, B. Cabrera and A. Miller, "The Atacama B-Mode Search: CMB Polarimetry with Transition-Edge-Sensor Bolometers", 2009.
- [27] C. Bischoff, A. Brizius, I. Buder, Y. Chinone, K. Cleary, R. Dumoulin, A. Kusaka, R. Monsalve, S. Næss, L. Newburgh, G. Nixon, R. Reeves, K. Smith, K. Vanderlinde, I. Wehus, M. Bogdan, R. Bustos, S. Church, R. Davis, C. Dickinson, H. Eriksen, T. Gaier, J. Gundersen, M. Hasegawa, M. Hazumi, C. Holler, K. Huffenberger, W. Imbriale, K. Ishidoshiro, M. Jones, P. Kangaslahti, D. Kapner, C. Lawrence, E. Leitch, M. Limon, J. McMahan, A. Miller, M. Nagai, H. Nguyen, T. Pearson, L. Piccirillo, S. Radford, A. Readhead, J. Richards, D. Samtleben, M. Seiffert, M. Shepherd, S. Staggs, O. Tajima, K. Thompson, R. Williamson, B. Winstein, E. Wollack and J. Zwart, "THE Q/U IMAGING EXPERIMENT INSTRUMENT", *The Astrophysical Journal*, vol. 768, no. 1, p. 9, 2013.
- [28] H. Tran, B. Johnson, M. Dragovan, J. Bock, A. Aljabri, A. Amblard, D. Bauman, M. Betoule, T. Chui, L. Colombo, A. Cooray, D. Crumb, P. Day, C. Dickenson, D. Dowell, S. Golwala, K. Gorski, S. Hanany, W. Holmes, K. Irwin, B. Keating, C. Kuo, A. Lee, A. Lange, C. Lawrence, S. Meyer, N. Miller, H. Nguyen, E. Pierpaoli, N. Ponthieu, J. Puget, J. Raab, P. Richards, C. Satter, M. Seiffert, M. Shimon, B. Williams and J. Zmuidzinas, "Optical design of the EPIC-IM crossed Dragone telescope", *Space Telescopes and Instrumentation 2010: Optical, Infrared, and Millimeter Wave*, 2010.
- [29] R. Hills, "Holography Measurement of a Two-Mirror System.", 2017.
- [30] S. Parshley, M. Niemack, R. Hills, S. Dicker, R. Dunner, J. Erler, P. Gallardo, J. Gudmundsson, T. Herter, B. Koopman, M. Limon, F. Matsuda, P. Mauskopf, D. Riechers, G. Stacey and E. Vavagiakis, "The optical design of the six-meter CCAT-prime and Simons Observatory telescopes", *Ground-based and Airborne Telescopes VII*, 2018.
- [31] B. Saleh and M. Teich, *Fundamentals of photonics*. Chicester: Wiley, 2013.
- [32] "OpticStudio Homepage - Zemax", Zemax.com, 2019. [Online]. Available: <https://www.zemax.com/products/opticstudio>. [Accessed: 29- Jan- 2019].
- [33] "GRASP - for reflector antenna analysis and design - TICRA", TICRA, 2018. [Online]. Available: <https://www.ticra.com/software/grasp/>. [Accessed: 17- Dec- 2018].
- [34] K. Pontoppidan, Technical description of GRASP 7 and GRASP C. Cph.: TICRA, 1993.
- [35] E. Purcell, *Electricity and Magnetism*, 2nd ed. Cambridge: Cambridge University Press, 2011.

# Chapter 8

## Appendix

```
import numpy as np
import matplotlib
import matplotlib.pyplot as plt
import matplotlib.tri as tri

def Correlator(Ref, Sig):
    N=Ref.N
    aux=np.zeros((N,N))
    aux=Ref.data*np.conjugate(Sig.data)
    Meas_Pattern=BeamPattern(aux, Sig.step, Sig.N, Sig.freq)
    return Meas_Pattern

def Resta(data1, data2):
    if (data1.N==data2.N and data1.step==data2.step):
        data=data1.data-data2.data
    else:
        data=[]
    U=SurfaceError(data, data1.mask, data1.step, data1.N)
    return U

def Suma(data1, data2, data3, data4):
    data=data1.data+data2.data+data3.data+data4.data
    U=SurfaceError(data, data1.mask, data1.step, data1.N)
    return U

def generateBP(pattern1, pattern2, ideal):
    data=pattern1.data+pattern2.data-ideal.data
    U=BeamPattern(data, pattern1.step, pattern1.N, pattern1.freq)
    return U

class Data_2D:
    def __init__(self, Data, step, N):
        self.N=N
        self.step=step
        self.data=Data

    def Gaussian(self, sigma):
        N=self.N
        self.data=np.zeros((N,N))
        aux=np.zeros((N,N))
        Kte=(sigma/self.step)**2
```

```

x0= (N/2+0.5)
y0= (N/2+0.5)
for i in range(N):
    for j in range(N):
        d2=((i-x0)**2+(j-y0)**2 )
        amplitude= np.exp(-(d2/Kte))
        aux[i ,j]=amplitude
self.data=aux+0j

def Uniform(self):
    N=self.N
    self.data=np.zeros((N,N))
    aux=np.zeros((N,N))
    for i in range(N):
        for j in range(N):
            aux[i ,j]= 1
    self.data=aux+0j

def Truncate(self ,R):
    N=self.N
    R2=(R/self.step)**2
    x0= (N/2-0.5)
    y0= (N/2-0.5)
    for i in range(N):
        for j in range(N):
            d2=((i-x0)**2+(j-y0)**2 )
            if d2>R2:
                self.data[i ,j]=0

def Map(self ,size):
    N=int(size)
    if (N>self.N): return
    N0=int(( self.N-N)/2)
    aux=np.zeros((N,N))+0j
    for i in range(N):
        for j in range(N):
            aux[i ,j]=self.data[N0+i ,N0+j]
    self.data=aux
    self.N=N

def Mask(self ,R):
    N=self.N
    R2=(R/self.step)**2
    x0= (N/2+0.5)
    y0= (N/2+0.5)
    for i in range(N):
        for j in range(N):
            d2=((i-x0)**2+(j-y0)**2 )
            if d2<R2:
                self.data[i ,j]=0

def plot(self ,string ,units):
    Data=self.data
    step=self.step
    N=self.N

```

```

if string=='ANG':
    U=np. angle (Data)
    title='Angle□[rad]'
elif string == 'dB':
    U=20*np. log10 (np. abs (Data))
    title='Power□[dB]'
elif string == 'Error':
    U=np. real (Data)*1E6
    title='Error□[um]'
else:
    U=np. abs (Data)
    title='Magnitude'
limits=((-step*N)/2,(step*N)/2,(-step*N)/2,(step*N)/2)
x, y = np. mgrid [limits [0]:limits [1]:273j, limits [2]:limits
[3]:273j]
x=np. reshape (x,N*N)
y=np. reshape (y,N*N)
U=np. reshape (U,N*N)
return plt. figure (1), plt. gca (). set _aspect ('equal'), plt.
    tricontourf (x[0:74528],y[0:74528],U[0:74528],200,cmap=plt.
    cm. jet), plt. colorbar (), plt. xlabel (units), plt. ylabel (
    units), plt. title (title)
#extent = (-step*N/2, step*N/2, -step*N/2, step*N/2)
#fig, ax = plt. subplots ()
#im = ax. imshow (np. abs (U), extent=extent)
#ax. set (xlabel=units, ylabel=units, title=title)
#X=np. linspace (-step*N/2, step*N/2, N)
#cs = ax. contourf (X,X,U,20)
#cbar = fig. colorbar (cs)
#plt. show ()
#return fig, ax

def plot _cut (self, string, units):
    N=self. N
    step=self. step
    index=int (N/2)
    x=np. arange (-N/2*step, N/2*step, step)
    if string=='ANG':
        y=np. angle (self. data [index, :])
    elif string == 'dB':
        y=20*np. log10 (np. abs (self. data [index, :]))
    elif string == 'Error':
        y=np. real (self. data [index, :]) *1E6
        title='Error□[um]'
    else:
        y=np. abs (self. data [index, :])
    fig, ax = plt. subplots ()
    ax. plot (x, y)
    ax. set (xlabel=units, ylabel=string)
    ax. grid ()
    return fig

def Save (self, name):
    np. savetxt (name, self. data, delimiter="," )

def Normalize (self):
    self. data=self. data /np. amax (np. abs (self. data))

```



```

def add_Noise(self , power):
    power=power*np.amax(np.abs(self.data))
    N=self.N
    for i in range(N):
        for j in range(N):
            noise= power*complex(np.random.normal(),np.
                random.normal())
            self.data[i , j]+=noise

def FFT(self):
    U=self.data
    n=self.N
    aux1=np.fft.fftshift(U)
    aux2=np.fft.fft2(aux1)
    aux3=np.fft.ifftshift(aux2)
    step=1/(self.N*self.step)
    P=Data_2D(aux3 , step , n)
    return P

def iFFT(self):
    U=self.data
    n=self.N
    aux1=np.fft.ifftshift(U)
    aux2=np.fft.ifft2(aux1)
    aux3=np.fft.fftshift(aux2)
    step=1/(self.N*self.step)
    P=Data_2D(aux3 , step , n)
    return P

class Illumination(Data_2D):
    def __init__(self , Data , step , N , freq):
        self.N=N
        self.step=step      #in [m]
        self.data=Data
        self.freq=freq      #in [Hz]
        self.size=N*step
    def __copy__(self):
        U=Illumination(self.data , self.step , self.N , self.freq)
        return U
    def plot(self , string):
        if string=='Error':
            string = 'ABS'
        p=super().plot(string , 'distance_□[m]' , )
        return p
    def plot_cut(self , string):
        p=super().plot_cut(string , 'distance_□[m]' , )
        return p
    def Save(self , name):
        p=super().Save(name)
        return p
    def Calculate_BeamPattern(self):
        U=Data_2D(self.data , self.step , self.N)
        b=U.FFT()
        lam=3E8/self.freq
        step_ang=lam*b.step*(180/np.pi)

```

```

        P=BeamPattern((b.data),step_ang,b.N,self.freq)
        return P
def Calculate_SurfaceError(self):
    lam=3E8/self.freq
    data=np.angle(self.data)*lam/(2*np.pi)
    P=SurfaceError(data,[],self.step,self.N)
    return P

class BeamPattern(Data_2D):
def __init__(self,Data,step,N,freq):
    self.N=N
    self.step=step #[deg]
    self.data=Data
    self.freq=freq #[Hz]
    self.size=N*step
def __copy__(self):
    U=BeamPattern(self.data,self.step,self.N,self.freq)
    return U
def plot(self,string):
    if string=='Error':
        string = 'ABS'
    p=super().plot(string,'angle_□[deg]')
    return p

def plot_cut(self,string):
    p=super().plot_cut(string,'angle_□[deg]')
    return p
def Save(self,name):
    p=super().Save(name)
    return p
def Calculate_Illumination(self):
    U=Data_2D(self.data,self.step*np.pi/180,self.N)
    b=U.iFFT()
    lam=3E8/self.freq
    step_lin=lam*b.step
    P=Illumination((b.data),step_lin,self.N,self.freq)
    return P

class SurfaceError(Data_2D):
def __init__(self,data,mask,step,N):
    self.N=N
    self.step=step #[deg]
    self.data=data #data should be real
    self.size=N*step
    self.mask=np.ones((N,N))
def __copy__(self):
    U=Illumination(self.data,self.mask,self.step,self.N)
    return U
def set_mask(self,mask):
    self.mask=mask #should be logic array (0 or 1)
    self.data=self.data*mask
def plot(self):
    p=super().plot('Error','distance_□[m]')
    return p

```

```

def plot_cut(self, string):
    p=super().plot_cut(string, 'distance_□[m] ')
    return p
def Save(self, name):
    p=super().Save(name)
    return p
def Normalize(self):
    n=np.sum(self.mask==1)
    self.data = self.data - np.sum((self.data))/(n)
    self.data=self.data*self.mask
def RMS(self):
    n=np.sum(self.mask==1)
    N=self.N
    data=self.data
    RMS= (np.sum(data*data))**0.5/(n)
    return RMS
def Saturate(self, min, max):
    N=self.N
    for i in range(N):
        for j in range(N):
            if self.data[i, j]>max:
                self.data[i, j]=max
            if self.data[i, j]<min:
                self.data[i, j]=min
def shiftax(self, distance, axe):
    shift=int(np.round(distance/self.step))
    datashift=self.data
    datashift1=np.zeros([self.N, self.N])
    if axe=="y":
        for i in range(self.N):
            datashift1[i]=np.concatenate((datashift[i][-
                shift:], datashift[i][: -shift]))
    if axe=="x":
        for i in range(self.N):
            datashift1[:, i]=np.concatenate((datashift[:, i
                ][-shift:], datashift[:, i][: -shift]))
    U=SurfaceError(datashift1, self.mask, self.step, self.N)
    return U

```